STRUCTURAL BIOLOGY

Autoinhibition and activation mechanisms revealed by the triangular-shaped structure of myosin Va

Fengfeng Niu[1,2]*†, Yong Liu[1,2,3]†, Kang Sun[1,2]†, Shun Xu[1,2], Jiayuan Dong[1,2], Cong Yu[2,4], Kaige Yan[2], Zhiyi Wei[1,2]*

As the prototype of unconventional myosin motor family, myosin Va (MyoVa) transport cellular cargos along actin filaments in diverse cellular processes. The off-duty MyoVa adopts a closed and autoinhibited state, which can be relieved by cargo binding. The molecular mechanisms governing the autoinhibition and activation of MyoVa remain unclear. Here, we report the cryo–electron microscopy structure of the two full-length, closed MyoVa heavy chains in complex with 12 calmodulin light chains at 4.78-Å resolution. The MyoVa adopts a triangular structure with multiple intra- and interpolypeptide chain interactions in establishing the closed state with cargo binding and adenosine triphosphatase activity inhibited. Structural, biochemical, and cellular analyses uncover an asymmetric autoinhibition mechanism, in which the cargo-binding sites in the two MyoVa heavy chains are differently protected. Thus, specific and efficient MyoVa activation requires coincident binding of multiple cargo adaptors, revealing an intricate and elegant activity regulation of the motor in response to cargos.

INTRODUCTION

Intracellular cargo transport is fundamental for cellular functions, which is driven by molecular motors, including actin-based unconventional myosins and microtubule-based kinesins and dyneins (1–5). Class V myosins (MyoVs), including MyoVa, MyoVb, and MyoVc in mammals and Myo2p and Myo4p in yeast, are ubiquitously expressed, processive motors for transporting highly diverse cellular components (e.g., vacuole, vesicles, melanosome, organelles, and mRNA) (6, 7). Mutations of human *MYO5a* and *MYO5b* genes are known to cause a broad spectrum of genetic diseases including Griscelli syndrome and microvillus inclusion disease (8, 9).

As one of the earliest identified and best-characterized unconventional myosins, MyoVa has been widely studied as a prototypic model to understand motor-mediated intracellular cargo transport (10, 11). MyoVa functions as a dimer for processive walking on actin filaments (7). It contains a motor domain (MD) in the N-terminal head that attaches to F-actin and hydrolyses adenosine 5′-triphosphate (ATP) to fuel mechanical movements, followed by six IQ motifs that bind to six calmodulin (CaM) molecules to form a lever arm (LA) for step-size amplification, a long coiled coil (CC) in the middle region that is responsible for dimerization, and a C-terminal tail region consisting of alternatively spliced exons and a globular tail domain (GTD) that recognizes cargos or cargo adaptors (10, 12) (Fig. 1A).

MyoVa can adopt an open/extended and closed/folded conformations. With loaded cargos, MyoVa in the open state has full adenosine triphosphatase (ATPase) activity and can walk along F-actin. Without cargos, the C-terminal GTD folds back to the N-terminal MD of MyoVa forming the closed and ATPase activity–inhibited state that loses the motility capacity (13–15). Biochemical studies have suggested that both the CC and the GTD are involved in the regulation of autoinhibition, and cargo plays a crucial role in activating MyoVa (16–19). Previous electron microscopic (EM) studies of the closed state revealed a unique triangular structure (16, 20), and several similar models were proposed later (21–24). However, the limited resolution (~24 Å) and tentative positioning of the MD, CC, and GTD in the EM map have limited the understanding of the molecular basis underlying the closed state formation and cargo-mediated activation of MyoVa. Although previous structural and biochemical studies of GTD suggest that the GTD may form a dimer and play a role in the cargo-induced MyoVa activation (19, 23–25), the underlying mechanism is still elusive.

Here, we solved a 4.78-Å cryo-EM structure of the full-length MyoVa-CaM complex in the closed state, revealing the unprecedented details of the interactions between the head and tail, the CaM and CC, and the CC and GTD, as well as the inhibited conformation of the head. In the complex, each GTD extends its N-terminal strand to the cargo-binding site of the neighboring GTD, forming a GTD dimer with their cargo-binding sites sealed as previously seen in the MyoVb-GTD crystal structure (23). Strikingly, the tail of the CC only interacts with one GTD and further stabilizes the sealed structure in this GTD, indicating an asymmetric cargo-mediated activation mechanism of MyoVa. Together with our biochemical and cellular evidences, the MyoVa structure allows us to build a model depicting how MyoVa may respond to different regulatory inputs to ensure proper cargo transport. Our structure of MyoVa in its closed state also provides insights on the autoinhibition of other members of the MyoVs.

[1]Brain Research Center, School of Life Sciences, Southern University of Science and Technology, Shenzhen, Guangdong, China. [2]Department of Biology, School of Life Sciences, Southern University of Science and Technology, Shenzhen, Guangdong, China. [3]SUSTech-HIT Joint PhD Program, Harbin Institute of Technology, Harbin, Heilongjiang, China. [4]Guangdong Provincial Key Laboratory of Cell Microenvironment and Disease Research and Shenzhen Key Laboratory of Cell Microenvironment, Shenzhen, Guangdong, China.
*Corresponding author. Email: weizy@sustech.edu.cn (Z.W.); niuff@sustech.edu.cn (F.N.)
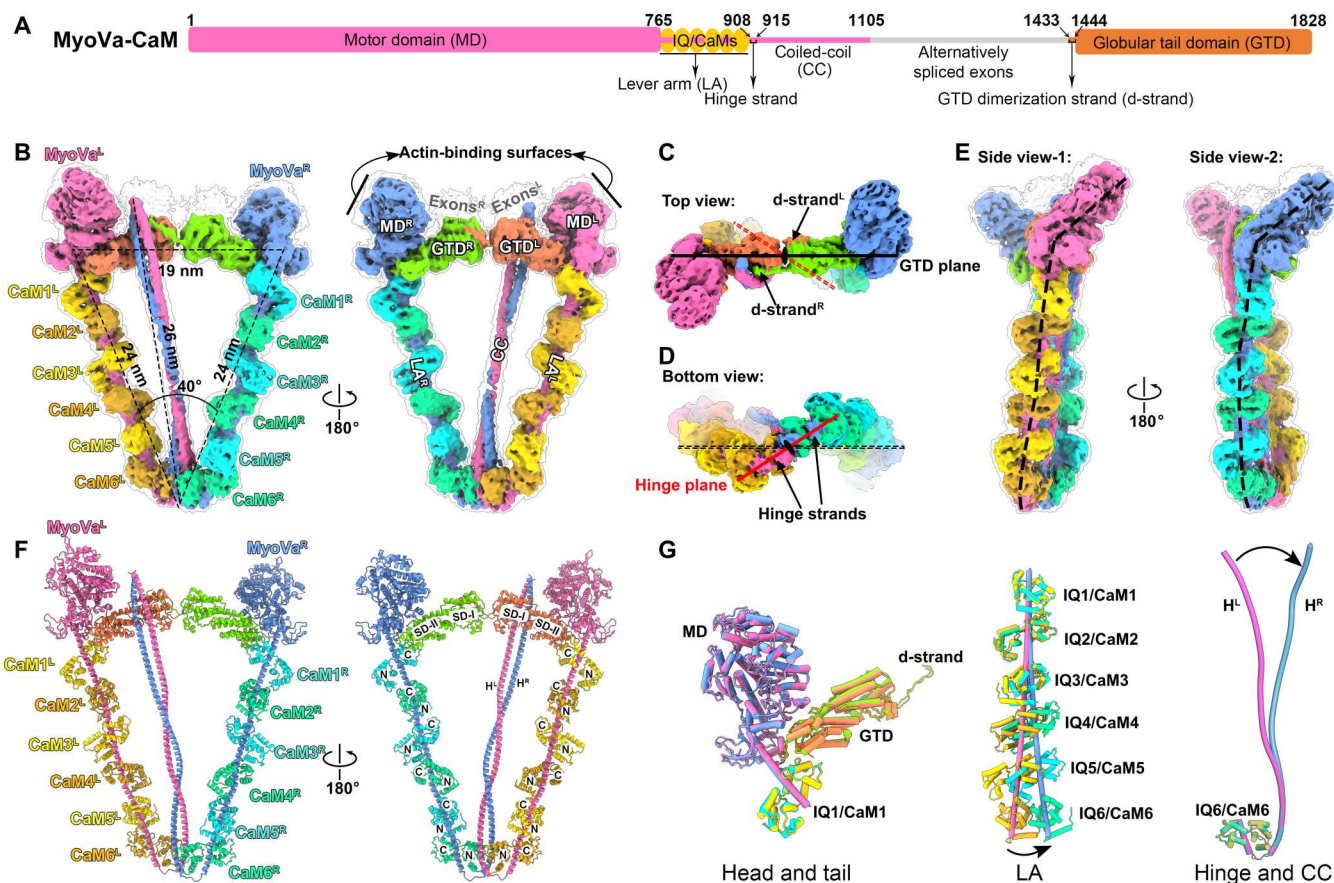†These authors contributed equally to this work.

Fig. 1. Overall structure of the closed MyoVa-CaM⁴ᴹ complex. (**A**) Schematic representation of the MyoVa-CaM complex. The domains of MyoVa and six CaM molecules are indicated. (**B**) Cryo-EM map of the MyoVa-CaM⁴ᴹ complex in the closed state, colored by different molecules. Two GTDs from the two MyoVa heavy chains are independently colored because of the undefined connection to the CC. The triangular shape is highlighted with the indicated lengths of three sides. (**C** to **E**) Top and bottom views (C and D) and two side views (E) of the cryo-EM map show the twisted triangular shape of the MyoVa-CaM⁴ᴹ complex. The density of two d-strands for GTD dimerization and two hinge strands for the CC reverse is labeled. The GTD plane, hinge plane, the twofold symmetric axis, and two long sides with different curvatures are indicated. (**F**) Atomic model of the MyoVa-CaM⁴ᴹ complex. All molecules or domains are colored with the same code as shown in (B). SD-I/SD-II of the GTDs, the two helices of the CC, and the N-/C-lobe of CaM are indicated. (**G**) Structural comparisons of the head/tail, LA, and hinge/CC regions between MyoVaᴸ and MyoVaᴿ. The two LAs and the hinge and CC regions are compared by aligning the IQ1/CaM1 and the IQ6/CaM6, respectively.

RESULTS

Overall architecture of the MyoVa-CaM complex in the closed state

We successfully expressed and purified mouse brain isoform MyoVa with CaM in high quality (fig. S1, A and B). Consistent with previous reports (*13–15*), MyoVa shows a higher tendency to fold as a triangular conformation in low salt buffer condition (fig. S1B). However, the amount of the compact MyoVa-CaM particles was still very limited (fig. S1B). To eliminate the disruptive effect of Ca²⁺ on the closed form (*13–15*), we coexpressed MyoVa with the Ca²⁺ binding–deficient CaM mutant (CaM⁴ᴹ) (*15*) and purified the MyoVa-CaM⁴ᴹ complex under low salt condition, which increased the fraction of the closed complex (fig. S1C). Cross-linking with glutaraldehyde (GA) was applied to further stabilize the closed MyoVa (fig. S1, D and E). We obtained a cryo-EM map of the MyoVa-CaM⁴ᴹ complex with 5.90-Å resolution refined using ~100,000 particles with relatively complete triangular shape from more than 30,000 micrographs (fig. S2). On the basis of this map and previous structural studies (*22, 26*), we predicted that a

V1437F substitution of MyoVa may strengthen the closed state (fig. S3; see the "Interface-II: The GTD dimer formation" section for details). The negative stain EM analysis of the MyoVaᵛ¹⁴³⁷ᶠ-CaM⁴ᴹ complex confirmed the increase of the closed state (fig. S3F), and cryo-EM analysis with more than 20,000 micrographs yielded an improved map (fig. S4). Last, the particles from MyoVa-CaM⁴ᴹ and MyoVaᵛ¹⁴³⁷ᶠ-CaM⁴ᴹ were combined to generate a final map with an overall resolution of 4.78 Å (fig. S5A and movie S1), and three subregions were further improved to higher resolutions of ~4.0 to 4.6 Å by using local refinement, respectively (fig. S5B). On the basis of these maps and the previously determined or AlphaFold2-predicted fragment structures of the MD (*27*), IQ/CaM (*28*), GTD (*26*), and CC (*29*), we successfully built the atomic model of the MyoVa-CaM⁴ᴹ complex in the closed state (fig. S5, C and D; table S1; and movie S1).

The closed MyoVa-CaM⁴ᴹ complex, containing 2 MyoVa (MyoVaᴸ and MyoVaᴿ, where the superscript "L" and "R" hereafter indicate the left and right position in the structure, respectively, as shown in left panel of Fig. 1B) and 12 CaM⁴ᴹ molecules, adopts a

shape close to an isosceles triangle with three side lengths of about 19 nm by 24 nm by 24 nm (Fig. 1, B to E). In this triangular structure, the two MDs (MD^L and MD^R) are located at the two top vertices with their actin-binding surfaces facing outside (Fig. 1, B and F). The two MDs and their following LAs (LA^L and LA^R) compose the two long sides forming an angle of ~40° between them, while two GTDs (GTD^L and GTD^R) are close to each other in a line to form the short side with two MDs (Fig. 1, B and F). In each long side, the LA is formed by six CaM molecules (CaM1 to CaM6) wrapping along the long helix consisting of six IQ motifs (IQ1 to IQ6) (Fig. 1, B and F), in which each CaM adopts a typical IQ-binding mode (fig. S6A) (28). At the bottom vertex, the region connecting the IQ6 and CC folds as a structurally defined strand (named hinge-strand hereafter; Fig. 1D), and the dimeric CC is sandwiched by the two CaM6 molecules at the very C-terminal ends of the two LAs (Fig. 1, B and F). This hinge-like conformation allows the fully extended CC to take a sharp bend with respect to LAs and fold back toward the short side of the triangle, thus positioning the two GTDs to closely contact with two MDs for the head/tail interactions. In the short side, although the two GTDs do not directly contact each other (Fig. 1, B and F), they are dimerized through a strand (named d-strand hereafter) extended from the N terminus of one GTD to latch onto the subdomain-I (SD-I) of the neighboring GTD (Fig. 1, C and F). This head-to-head dimerization

of the two GTDs positions the SD-II to be trapped by the MD and LA in each side (Fig. 1F).

$MyoVa^L$ and $MyoVa^R$ are highly symmetric in both the top side and bottom vertex (Fig. 1, C, D, and G). However, the plane across two GTDs (GTD plane) and that across two hinge strands (hinge plane) are mismatched, resulting in the twisted triangular shape (Fig. 1, C and D, and movie S1). This twist is also reflected by the slightly different conformations of the two LAs: The LA^L is relatively straight, while the LA^R has an ~10° bend starting at IQ2 (Fig. 1, E and G, and movie S1). The bend allows the N-terminal and C-terminal ends of the LA^R connecting to the mismatched GTD and hinge planes, respectively. The small conformational difference between two LAs suggests that LAs have both rigidity and flexibility in shaping the twisted triangular shape. The rigidity of the LA is mainly maintained by the inter-CaM interactions, especially the CaM1/2, CaM3/4, and CaM5/6 interactions (fig. S6B), consistent with the crystallographic study of the IQ1-2/CaM1-2 (28). However, the interfaces between CaM2/3 and between CaM4/5 are very limited (fig. S6C), thereby providing certain flexibility for the LAs. The largest difference between $MyoVa^L$ and $MyoVa^R$ in the closed state occurs at the latter half of the CC (Fig. 1G), which generates a tilting of the CC toward the LA^L, consistent with the previous observations (16, 20). Consequently, the C-terminal region of the CC interacts only with one GTD (i.e., with the GTD^L but not GTD^R; Fig. 1, B and F), although the binding of the CC has minimal structural perturbation to the GTD (fig. S6D). Lowering the low contour level of the EM map reveals extra densities proximal to GTDs, which presumably correspond to the alternatively spliced exons between the CC and GTD (Fig. 1, A and B). Because of poor quality of the map of the connecting exons in our model, we cannot tell whether the MD and GTD interaction is intra- or interpolypeptide chain in nature in this closed MyoVa structure.

Comparison of our MyoVa-CaM complex structure to the previous structural observations
The current understanding of MyoVa autoinhibition is largely based on the triangular shape of the closed MyoVa indicated by a low-resolution cryo-EM map based on subtomogram averaging analysis for two-dimensional (2D) crystal on lipid monolayer and 2D negative stained EM image (16, 20, 21). Our structure can be nicely fitted into the map generated from 2D-crystallized MyoVa (fig. S6E) and closely resembles the averaged negative staining EM observation of the closed MyoVa isolated from mouse brain (fig. S6F). However, we found several misinterpretations or unobserved structure features in the previous studies (Fig. 2A), including the uncertain GTD orientation, due to the low-resolution map and the lack of available crystal structures at that time for map fitting.

The MD orientation in the previous EM model differs from those in our structure, and the GTD positions can only be vaguely described (Fig. 2B), thereby leading to the speculation that the GTD might block the MD activity by binding to the loop-1 near the active site of the MD (20). In addition, as the conformations of the MD and LA in the closed state of MyoVa cannot be clearly defined by the low-resolution observations, several different MD states have been proposed to be the inhibited MD conformation (16, 20). However, our structural analysis indicates that the inhibited MD adopts a unique conformation (see "The autoinhibition of ATPase activity in the closed state" section for details), differing from any proposed ones.
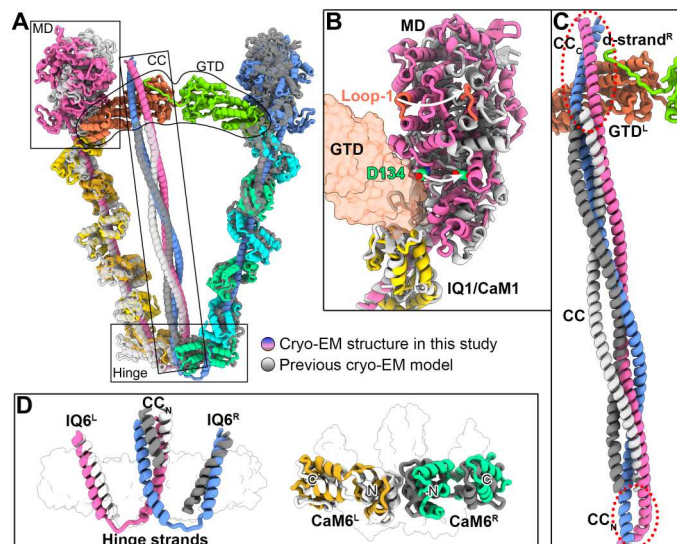

Fig. 2. Comparison of our MyoVa-CaM⁴ᴹ complex structure to the previous model. (**A**) Structural comparison of our model and the reported model [Protein Data Bank (PDB) ID: 2DFS] from a previous low-resolution map (~24 Å at FSC = 0.5). The GTD dimer in our model is indicated. The comparison of the MD, CC, and hinge regions are shown as zoom-in views in (B), (C), and (D), respectively. (**B**) Structural comparison of the MD^L regions in the two models. The GTD in our closed structure is showed with a transparent surface. D134 in the GTD-binding interface and the loop-1 close to the active site of MDs are highlighted, and their rotations between the two models are indicated by white arrows. (**C**) Structural comparison of the CC regions in the two models. The two ends of the CC that were not built in the previous model are indicated by two red dashed circles, respectively. (**D**) Structural comparison of the hinges in the two models. MyoVa heavy chain and CaM6 are highlighted in the left and right panels for the comparison, respectively. The N-lobe and C-lobe of CaM6 are indicated.

Because of the lack of structure features, the elongated CC structure is very difficult to be accurately assigned into a tube-like density in the previous EM map (fig. S6E). The partial CC region was placed as a typical CC in the previous autoinhibition model, which cannot satisfactorily explain the important role of the CC in regulating MyoVa's activity (17). By combining the AlphaFold2-based prediction (29), we confidently assigned the entire CC region into our cryo-EM map (fig. S5, C and D), which revealed the local unwinding of the C-terminal part of the CC (Fig. 2C) and the discontinued helical conformation between the LA and the CC via forming the hinge structure (Fig. 2D). The previously unassigned regions at the two ends of the CC play critical roles in the assembly of the autoinhibition conformation as described in detail below.

The interactions required for the closed state formation

To maintain the twisted triangle conformation in the closed state, the MyoVa-CaM^{4M} complex uses extensive interactions between different regions including the following: the head/GTD interaction (interface-I) mediated by the MD, CaM1, and GTD; the GTD dimerization (interface-II) mediated by the GTD and d-strand; the hinge interaction (interface-III) mediated by the CC and CaM6; and the GTD/CC interaction (interface-IV) (Fig. 3, A to C, and table S2). The interface-I, interface-II, and interface-III occur in both MyoVa^L and MyoVa^R, whereas the interface-IV is only formed between the GTD^L and CC. These interactions represent the complexity of inhibition/activation regulation of MyoVa. However, it should be noted that because of the limited resolution of our cryo-EM maps, some of side chain–involving interactions are potential rather than definitive contacts.

Interface-I: The head/GTD interaction

The head/tail interaction is critical for the autoinhibition of MyoVa. The N-terminal and the converter regions of the MD and the C-lobe of the CaM1 form a deep groove to tightly hold the GTD SD-II (interface-I; Fig. 3A). Conversely, the binding of the GTD to the MD and CaM1 locks the orientations of the MD and LA, preventing the LA from swinging. The head/GTD interaction buries an area of ~1200 Å^2 on the GTD surface, depicting the essential role of GTD in maintaining the closed state of MyoVa (16–18).

The MD/GTD interaction covers many surface residues, including D134 and D136 in the MD, which have been characterized as key sites for GTD-mediated suppression of ATPase activity (17, 18). In our structure, these two negatively charged residues are directly involved in the charge-charge interaction and hydrogen bonding with several positively charged residues (K1754, R1680, and K1681) in GTD (Fig. 3A, I-1). Hydrophobic interaction also plays a role in the GTD/MD interaction. Specifically, L1679^{GTD} and L1790^{GTD} interact with a hydrophobic surface patch on MD (Fig. 3A, I-2). In addition to the MD/GTD interaction, a loop (residues 1760 to 1770) in GTD is inserted into the cleft formed between the MD and CaM1, in which the C-lobe of the CaM1 directly binds to the GTD (Fig. 3A, I-3). The tight packing between the CaM1 and GTD explains the previous finding that the CaM1 is important in regulating the autoinhibited ATPase activity of MyoVa (30, 31).

Interface-II: The GTD dimer formation

In our structure, the two GTDs are aligned in a head-to-head manner through a twofold symmetry (Fig. 1C), posing the SD-IIs toward the MDs for the head/tail interaction (Fig. 1F). Although the two SD-Is from the two GTDs are close to each other, no

direct contact is found between them (Fig. 1, C and F). This observation raised a question on how the two GTDs may dimerize to maintain the stable structure of the short side of the triangular shape. After the initial model building, we found that a small patch of unexplained density becomes apparent on the SD-Is of both GTDs (fig. S3A). This unexplained density occupies a shallow groove of the SD-I, which is required for binding to the GTD-binding motifs (GTBMs) found in cargo adaptors such as melanophilin (Mlph) and Spires (23, 25, 26). As indicated by the previously crystallographic analysis of the GTD of MyoVb (23), this density may originate from the d-strand at the N-terminal extension of the GTD, which has been proposed to stabilize the GTD dimer in the closed state (fig. S3B) (19, 22, 23). As the N terminus of one GTD is near the GTBM-binding groove in the neighboring GTD due to the twofold symmetry (Fig. 1C), we modeled the d-strand (residues 1435 to 1443) extending from the GTD^R N terminus into the density on the GTD^L and vice versa (fig. S3C). However, the density quality is not good enough to assign the d-strands without ambiguity.

To improve the density quality and to validate our model, we strove to find a mutation that can enhance the GTD dimer in the closed state. Consistent with the previous observation, the d-strand and the GTBM share a similar binding mode, if their sequences are aligned in the reversed manner (fig. S3C) (23). V1437 in the d-strand is aligned with a phenylalanine in Mlph-GTBM (fig. S3C), which is critical for the binding of Mlph to GTD (23, 26). We postulated that the V1437F mutation may increase the hydrophobic interaction between the d-strand and GTD. Satisfyingly, V1437F promotes the GTD/d-strand interaction and GTD dimerization in solution (fig. S3, D and E), and MyoVa^{V1437F} has a higher propensity to adopt the closed state (fig. S3F). Adding particles obtained using the MyoVa^{V1437F}-CaM^{4M} complex, the EM density of not only the d-strands but also the entire complex was largely improved to support our model building (figs. S4 and S5).

In the interface-II, the binding of the d-strand to the GTBM-binding groove is mediated by both hydrophobic and charge-charge interactions (Fig. 3B, II-1). In addition to V1437$^{d\text{-strand}}$, I1439$^{d\text{-strand}}$ is involved in the hydrophobic packing with the groove, while R1441$^{d\text{-strand}}$ and K1442$^{d\text{-strand}}$ interact with the SD-I through hydrophilic interaction (Fig. 3B, II-1). As the dimer formation places the two GTDs at the right orientation for the head/tail interaction, the GTD/d-strand interaction mediates GTD dimerization and thereby contributes to the closed state formation of MyoVa.

Interface-III: The hinge formation

Through the short hinge strands, the CC takes a reversed direction with respect to the LAs and guides the head/tail interaction mediated between GTDs and MDs (Fig. 1, D and F). To stabilize the sharp turn of the hinge strand, the two CaM6 molecules at the two LA ends tightly sandwich the N-terminal part of the CC (CC$_N$), forming a stable hinge structure at the joint point between the two long sides of the triangular structure (Fig. 1, B and F). The CaM6/CC$_N$ interaction in the interface-III involves the N-lobe of CaM6 that is located on the opposite side of the IQ motif binding surface of CaM (Figs. 1F and 2C), representing another unique CaM/target interaction mode. The CC$_N$-binding site involves a cluster of hydrophobic residues from the N-terminal loop and the first and fourth helices of the CaM6 N-lobe, which form a
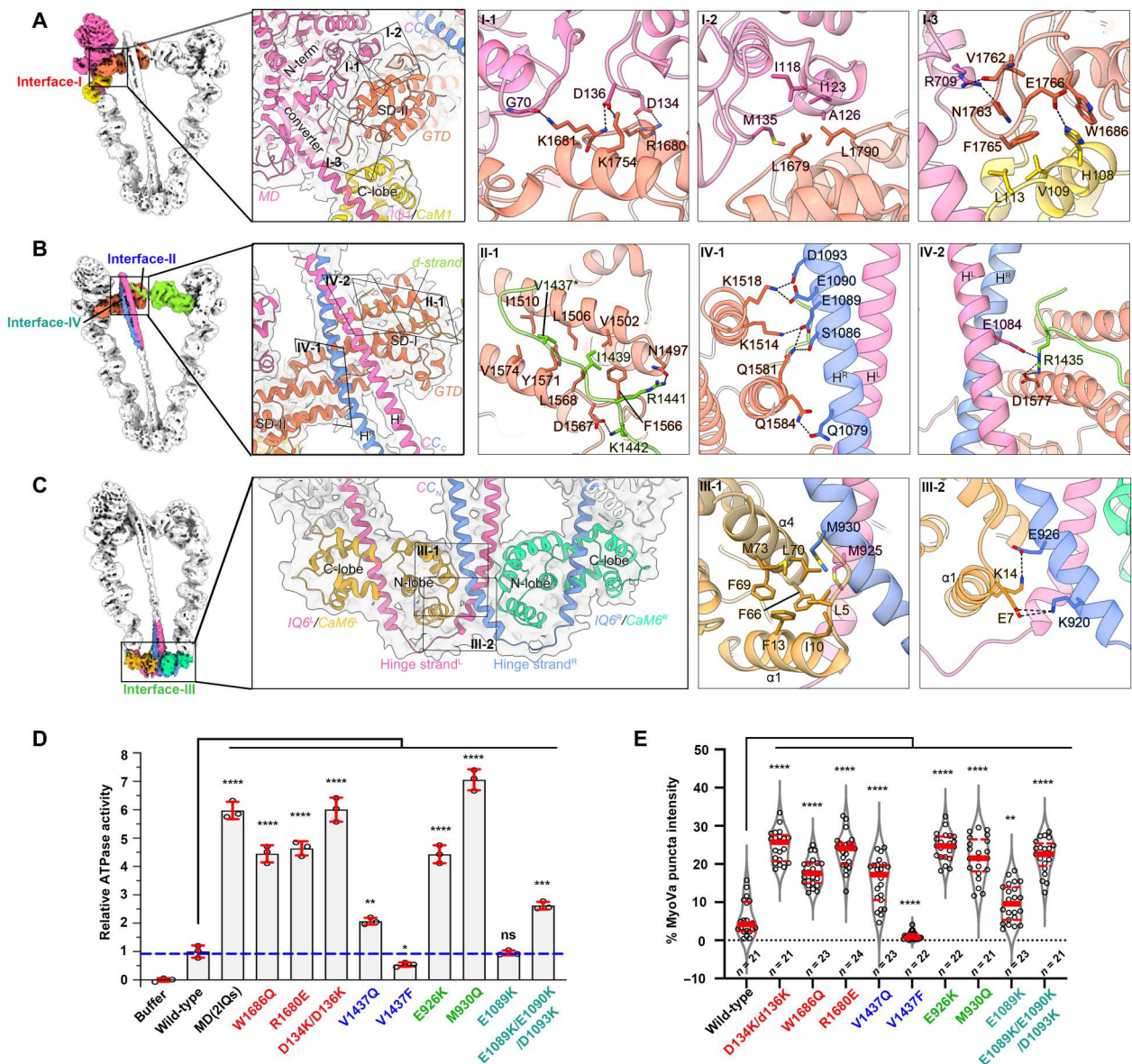
Fig. 3. The interactions in the formation of the closed MyoVa-CaM^{4M} complex. (**A** to **C**) The four interfaces in the MyoVa-CaM^{4M} complex, including the interface-I between MD^L/CaM1^L and GTD^L for the head/GTD interaction (A), the interface-II between GTD^L and d-strand^R for the GTD dimerization (B), the interface-III between IQ6/CaM6 and CC$_N$ for the hinge formation (C), and the interface-IV between GTD^L and CC$_C$ (B). The molecular details of these interfaces are presented in zoom-in views with the interacting residues shown in stick mode. Hydrogen bonds and salt bridges are indicated as dashed lines. V1437 that was mutated to phenylalanine for structure determination is labeled with an asterisk. (**D**) The ATPase activity analysis of the wild-type and mutated MyoVa in complex with CaM. The MD(2IQs) was used to indicate the fully activated MD. All measured activity values were normalized to that of the wild-type MyoVa for comparison. All the reactions were experimentally repeated three times in this and the following measurements of ATPase activity. (**E**) Statistical analysis of the puncta formation of MyoVa or its mutants in the HeLa cells. The representative imaging data are shown in fig. S8C. Cell number for each condition investigated is indicated. The mutations locating in interfaces I to IV are respectively labeled with different color in (D) and (E), corresponding to the interfaces I to IV indications in (A) to (C). ns, not significant.

hydrophobic pocket to accommodate M925 and M930 in CC$_N$ (Fig. 3C, III-1). In addition, several residues (e.g., E7^{CaM6} and K14^{CaM6}) surrounding this pocket form salt bridges with K920 and E926 in CC$_N$ (Fig. 3C, III-2). The extensive association between CaM6 and CC$_N$ not only fixes the CC orientation to maintain the hinge formation but also firmly links the two LA ends to stabilize the triangular shape. The hinge structure must be

disassembled upon MyoVa activation, so that the CC can extend away from the MD in the open MyoVa (*32*).

Interface-IV: The GTD/CC interaction
Although the two CaM6/CC$_N$ interfaces are highly similar (Fig. 1G), the long CC in the middle of the structure is gradually tilted away from the central line of the triangle (Fig. 1B). Consequently, the C-terminal part of the CC (CC$_C$) attaches to the GTD^L (Fig. 1F). Unlike the typical CC conformation seen in the

N-terminal half of the CC that forms a two-turn superhelix, the CC_C spans ~8 nm without forming superhelix, resulting in a parallel-like association between the two helices (H^L and H^R) from $MyoVa^L$ and $MyoVa^R$, respectively (Fig. 1, F and G). It is likely that the binding of CC_C to GTD^L stabilizes the unique conformation of CC_C, as the C termini of the H^L and H^R extending beyond the GTD^L coil with each other again (Fig. 1F). In CC_C, the H^L is straight and has a very limited contact with the GTD^L, whereas the H^R has a kink in the middle (Fig. 1G) that allows the H^R to pack with the GTD^L more closely than the H^L (Fig. 2B, interface-IV). The CC-binding site is located on a positively charged surface of the SD-I in the GTD^L (Fig. 1F and fig. S7A), which complimentarily interacts with several negatively charged residues ($E1089^{CC}$, $E1090^{CC}$, and $D1093^{CC}$) in the H^R [Fig. 3B (IV-1) and fig. S7A].

The CC-binding site is coupled with the d-strand–binding site in GTD^L (Fig. 1B). The N terminus of the d-strand^R extended from the GTD^R inserts into a deep cleft formed by the GTD^L and CC_C [Fig. 3B (IV-2) and fig. S7B]. In this cleft, R1435 in the d-strand^R interacts not only with D1577 in the GTD^L but also with $E1084^{CC}$ in the H^L (Fig. 3B, IV-2). As these charge-charge interactions are buried by the CC_C (fig. S7B), the GTD^L/d-strand^R interactions are further enhanced. Without the CC sheltering, the corresponding GTD^R/d-strand^L interaction is solvent-exposed and considerably weak, as indicated by no detectable binding of the d-strand to GTD using ITC (fig. S3D). The d-strand^L may temporarily dissociate from the GTD^R, resulting in wobbling of the GTD^R and its bound MD^R. The 3D classification results of all wild-type MyoVa particles reveal that more than one quarter of particles have a stable MD^L vertex with an unstable MD^R vertex (fig. S7, C and D). Nevertheless, the mobile GTD^R in these particles remains proximal to the GTD^L via the CC-stabilized d-loop^R/GTD^L interaction.

Considering the high conformational flexibility of long CCs, the respective binding of the two ends of the CC to CaM6 and GTD^L stabilize the CC orientation (Fig. 1B). Conversely, the CC provides an important linkage between the bottom/hinge vertex and the top/short side in the triangular structure to further stabilize the closed state of MyoVa. Consistent with our structural finding, deleting the majority part of the CC_C from MyoVa was reported to impair the closed structure formation (17).

Interface mutations affect the autoinhibition of MyoVa

To validate the importance of the four interfaces in maintaining the closed state, we introduced several interface mutations in MyoVa that presumably either stabilize (e.g., V1437F) or disrupt (the mutations other than V1437F) the closed state and analyzed the impacts of these mutations on the closed conformation of the motor. Unlike the relatively compact conformation of the wild-type MyoVa, most of the MyoVa mutants prefer the open/extended conformation as indicated by analytical gel filtration (fig. S8, A and B). By measuring the ATPase activity of MyoVa, we quantified the impact of each mutation in the interfaces on the autoinhibition. In agreement with the indispensable role of the head/tail interaction in the closed and inhibited state, the interface-I mutations (e.g., D134K/D136K and W1686Q) boost the ATPase activity to the level comparable to the fully active MyoVa fragment containing only the MD and the first two IQ motifs [named MD(2IQs)] (Fig. 3D). Similarly, the mutations at the interface-III in CC_N (E926K and M930Q) markedly elevate the ATPase activity of MyoVa (Fig. 3D), confirming that the hinge structure is critical

for the closed and autoinhibited conformation. Compared with the profound impairments to the autoinhibition by the interface-I and interface-III mutations, the interface-II and interface-IV mutations (e.g., V1437Q) show mild effects on the autoinhibition of MyoVa (Fig. 3D and fig. S8A), suggesting that the binding of the d-strand and the CC to the GTD play a secondary role in the closed state formation. In contrast, the V1437F mutation, which adopts a more compact conformation than the wild-type MyoVa (figs. S3F and S8A), has an even lower ATPase activity when compared to the wild-type MyoVa (Fig. 3D), confirming that the V1437F mutation can further stabilize the autoinhibited conformation of MyoVa.

In HeLa cells, consistent with the cellular punctate distribution of activated MyoVa reported previously (33, 34), all the interface mutants of MyoVa that disrupt the closed state show significantly more puncta formation than the wild-type MyoVa (Fig. 3E and fig. S8, C and D), whereas the V1437F mutant that stabilizes the closed state is diffused in the cytoplasm (Fig. 3E and fig. S8, C and D). In addition, we generated MyoVa knockout ($MyoVa^{KO}$) melanocytes to investigate the impacts of the mutations on MyoVa-mediated melanosome transport (fig. S9, A to C). Compared to the wild-type MyoVa, the D134K/D136K, V1437Q, and W1686Q mutants have the similar or slightly higher capability in dispersing melanosome to cell peripheries while the stronger puncta form (fig. S9, D and E). However, $MyoVa^{V1437F}$ only partially rescues the melanosome aggregation in the $MyoVa^{KO}$ melanocytes (fig. S9, D and E), indicating a reduced capacity of $MyoVa^{V1437F}$ in cargo binding and/or transport. Together, the cellular observations further validated our structural and biochemical findings.

The autoinhibition of ATPase activity in the closed state

To walk along actin filaments, MyoVa uses MD to perform a mechanochemical transition of energy from ATP hydrolysis (10). Force is generated during an ATP hydrolysis cycle catalyzed by MD, in which extensive rearrangements of the subdomains (N-terminal, U50, L50, and converter) regulate nucleotide binding/release, actin binding, and converter and LA swinging (Fig. 4A) (35, 36). A series of transition states occurs in the ATP hydrolysis cycle to generate powerstroke and support the step-by-step walking of MyoVa on F-actin (27, 37–39). Therefore, interrupting any transition in the ATPase cycle may inhibit the ATPase activity of MyoVa. Extensive biochemical and cellular studies have demonstrated that the head/tail interaction directly inhibits the ATPase activity of MyoVa (15, 17–19), albeit the inhibition mechanism remains unclear.

We compared the GTD-bound MD structure with the reported MD structures in the different transition states of the ATPase cycle, including rigor (nucleotide-free and F-actin binding)/rigor-like (nucleotide-free), post-rigor transition {adenosine-5'-[(β,γ)-imido]triphosphate (AMPPNP) and F-actin binding}, post-rigor [adenosine 5'-diphosphate (ADP)–BeF$_3$ binding], pre-powerstroke (ADP-VO$_4$ binding), and weak/strong ADP binding (ADP only/ADP and F-actin binding, respectively) states (27, 37–39). The structural comparison shows that the LA and active site conformations are different from any of the above-mentioned states (Fig. 4, B and C). In the closed state, the GTD dimer blocks both the two LAs from swinging by locking the orientations of both N-terminal and converter in the MD and CaM1 (Figs. 1F and 4A). Considering the incompatibility between the GTD binding and the LA movement
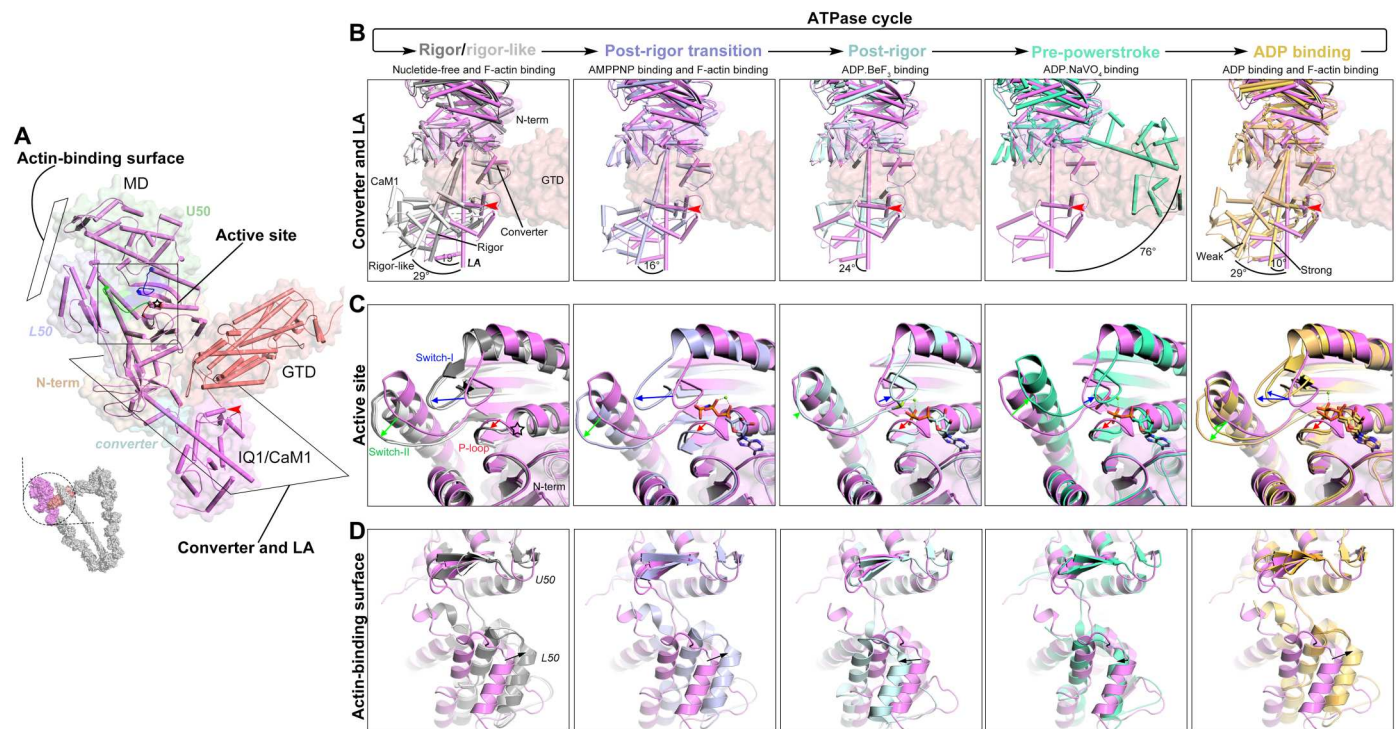
Fig. 4. Structural analysis of MD and its inhibition in the closed state. (**A**) GTD-bound MD structure in the closed MyoVa. The four subdomains, N-terminal, U50, L50, and converter in MD are indicated, which regulates the coupled conformational change of the actin-binding site, active site, and LA. In the active site, P-loop, switch-I, and switch-II, essential for ATP binding and hydrolysis, are colored in red, blue, and green, respectively. The nucleotide-binding site is marked by a star. The helix in CaM1 that binds to the GTD is indicated by a red arrowhead. (**B**) Structural comparisons of MD and LA in the closed state (GTD-bound) to those in rigor (PDB ID: 7PLT)/rigor-like (1OE9), post-rigor transition (7PMD), post-rigor (1W7J), pre-powerstroke (4ZG4), and weak/strong ADP-binding (1W7I and 7PM5) states within the ATPase cycle by aligning their N-terminal subdomains. The structural model of the pre-powerstroke state is generated by adding IQ1/CaM1 to the MyoVc-MD structure with the pre-power-stroke conformation. The LA rotation angles between the closed state and the other states are indicated. (**C**) Structural comparisons of active sites in the closed state and the states of the ATPase cycle showing the conformational changes of switch-I, switch-II, and P-loop. The bound nucleotides are shown in sticks. (**D**) Structural comparisons of actin-binding surfaces in the closed state, the different states in the ATPase cycle by aligning their subdomains of the U50 of the MD, and the conformational changes of the subdomain of the L50 are indicated.

within the ATPase cycle (Fig. 4B), the closed state occludes the ATPase cycle to inhibit the ATPase activity of MyoVa. In addition, compared with a series of transition states in the ATPase cycle, the P-loop, switch-I, and switch-II in the active site are positioned differently in the GTD-bound MD (Fig. 4C). Although no nucleotide was found in our EM map of the closed state (fig. S10), the switch-I and switch-II in the GTD-bound MD adopt the poses closer to those in the post-rigor state (Fig. 4C), suggesting that the GTD-bound MD prefers the ATP-bound conformation in the active site. Considering the high cellular concentration of ATP, the closed MyoVa in the physiological condition likely binds to ATP (*40*). Nevertheless, whether ATP binding may alter the MD conformation observed in our study requires further investigations. By aligning the U50 parts of the MDs in the different states, we found that the L50 position in the closed state resembles that in the pre-powerstroke state (Fig. 4D), which was suggested to have little capacity for actin binding (*36*). As U50 and L50 form the actin-binding surface (Fig. 4A), it is likely that the closed MyoVa cannot strongly bind to F-actin, consistent with the previous findings (*16*, *40*).

Activation mechanisms of the closed MyoVa

To transport cargo, MyoVa must be activated from the closed state to the open state. Cargo and calcium were considered as two major factors in activating MyoVa (*21*, *24*), although the activation mechanisms have not yet been decoded.

GTBM-binding mediated activation

Our structure confirms that the d-strand–mediated GTD dimerization is important for the closed state formation of MyoVa (Fig. 3, B and D). Several different cargo adaptors, including Mlph, MICAL1, and Spires, all use their GTBMs to recognize MyoVa via the GTBM-binding groove on GTD (*23*, *25*, *26*, *41*), which is occupied by the d-strand in the closed MyoVa (Fig. 5, A and B). The overlapped binding of the d-strand and GTBMs to the GTD immediately suggests a plausible mechanism for cargo-mediated activation, in which the GTBM interferes with the GTD/d-strand interaction upon cargo loading and thereby disrupts the d-strand–mediated GTD dimerization, leading to the opening of the closed state and release of the autoinhibition of MyoVa, as the previous proposed (*25*). The Mlph-GTBM peptide activates MyoVa in a dose-dependent manner in the ATPase assay (Fig. 5C) (*42*, *43*). However, very high concentrations (1000-fold or more than MyoVa) of the GTBM are required to release the autoinhibition of MyoVa in the ATPase
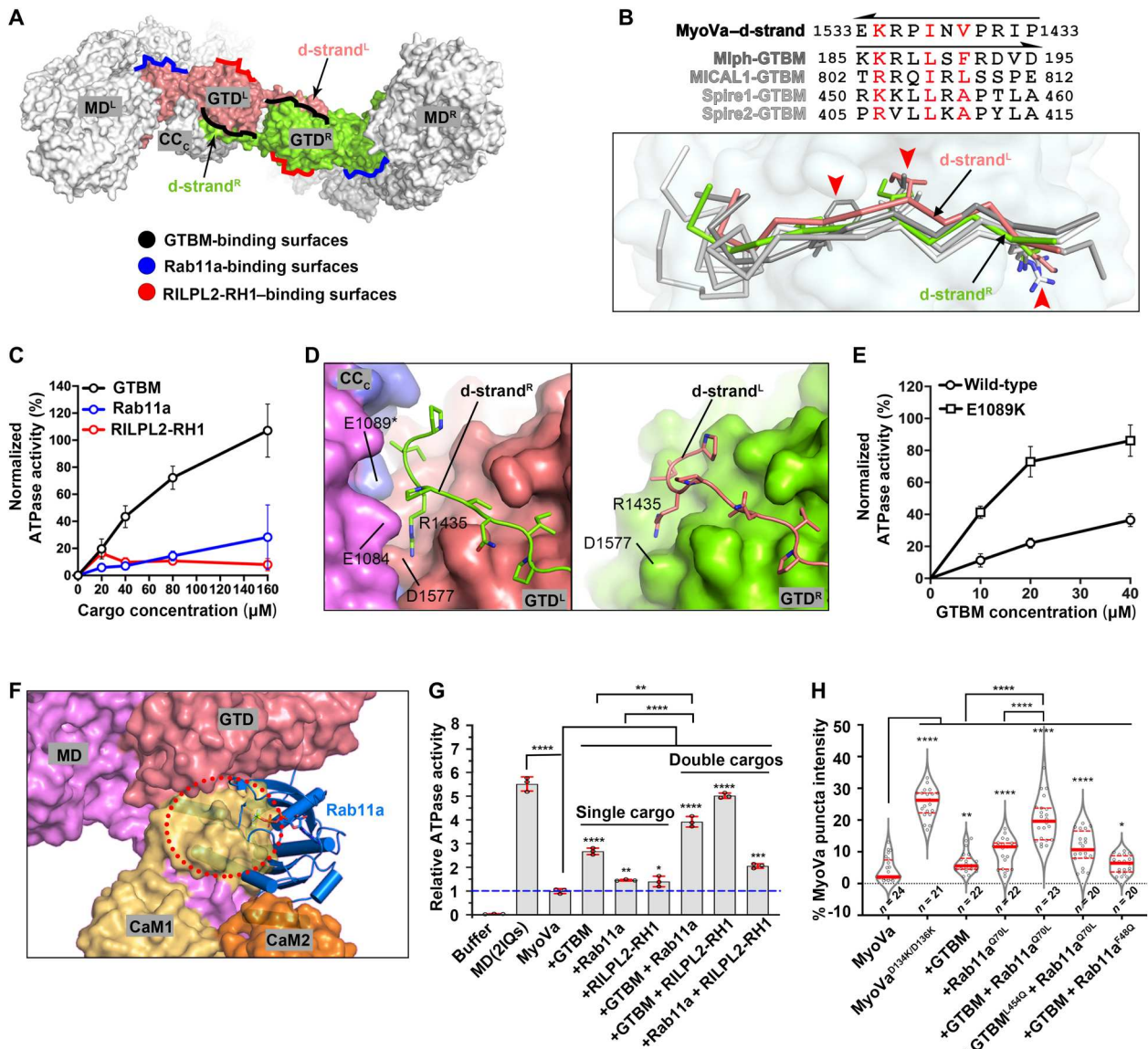
Fig. 5. Cargo-mediated MyoVa activation. (A) Three cargo-binding surfaces on the GTD that are blocked in the closed state. **(B)** Sequence and structural alignments of the d-strand in MyoVa and GTBMs in Mlph (PDB ID: 4KP3), MICAL1 (6KU0), and Spires (5JCY) by aligning the GTDs. The three key residues for GTD binding are highlighted. **(C)** ATPase activity of MyoVa (0.1 μM) measured with the different concentrations of indicated proteins. The activity was normalized to the conditions containing MyoVa and MD(2IQs) as 0 and 100%, respectively. Mlph-GTBM was used in this and the following ATPase assays. **(D)** Sheltering effect of CC_C on the GTD^L/d-strand^R, but not GTD^R/d-strand^L, interaction. **(E)** ATPase activities of MyoVa and MyoVa^{E1089K} (0.1 μM) in the presence of Mlph-GTBM. **(F)** Head/GTD interaction is disrupted by the binding of Rab11a to the GTD. The Rab11a-bound GTD (PDB ID: 5JCZ) is superimposed with that in the closed state. Clashes between the CaM1 and Rab11a are indicated by a dashed circle. **(G)** ATPase activity of MyoVa in the presence of individual cargo adaptors or their combinations. Concentrations of MyoVa and each cargo are of 0.1 and 40 μM, respectively. The ATPase activities were normalized with the same method used in Fig. 3D. **(H)** Statistical analysis of the punctate MyoVa in the HeLa cells coexpressing the wild-type MyoVa with either Spire1-GTBM or Rab11a^{Q70L} (a constitutively active form) or both Spire-GTBM and Rab11a^{Q70L}. The GTD binding-deficient mutants, Spire1-GTBM^{L454Q} and Rab11a^{F48Q}, were analyzed correspondingly. The indicated number of cells was selected for analysis in each condition.

assay (Fig. 5C), suggesting that GTBM binding alone is not sufficient for the effective activation of MyoVa.

The two GTD/d-strand interactions observed in our structure are different. The binding of the d-strand^R to GTD^L, but not the d-strand^L to GTD^R, is further enhanced by the CC_C (Fig. 5D). The CC-stabilized GTD^L/d-strand^R interaction should greatly elevate the threshold concentration for the GTBMs to compete with the d-strand in binding to the GTD. To investigate the

stabilization effect of CC_C on the GTD^L/d-strand^R interaction in the presence of GTBMs, we designed the E1089K mutation in the interface-IV to mildly weaken the CC_C/GTD^L interaction without losing the closed conformation. Although MyoVa^{E1089K} still shows the inhibited ATPase activity at the level comparable to that of the wild-type MyoVa (Fig. 3D), the mutation markedly increased the sensitivity of MyoVa^{E1089K} activation in responding to Mlph-GTBM (Fig. 5E), supporting the critical role of CC_C in

regulating MyoVa activation. Thus, the asymmetric binding of the CC to the GTD[L] in the closed state sets a very high concentration threshold for the GTBM-mediated activation of MyoVa.

Coincident activation by multiple cargo adaptors

In addition to the GTBM-containing proteins, Rab11a and Rab-interacting lysosomal protein-like 2 (RILPL2) are well-known cargo adaptors of MyoVa (44, 45). The Rab11a-binding surface on MyoVa-GTD partially overlaps with the GTD/CaM1 interface in our structure (25) (Fig. 5, A and F), suggesting that Rab11a may modulate the head/tail interaction and thereby facilitate the activation of MyoVa. Although the RILP homology 1 (RH1) domain of RILPL2 binds to a surface on GTD that is not involved in the closed state formation (Fig. 5A), the stable dimer structure of the RH1 domain of RILPL2 and its strong binding to GTD could potentially interfere with the d-strand–mediated GTD dimerization in the autoinhibited MyoVa (fig. S11, A and B) (26). Despite the potentially disruptive effects on the closed MyoVa formation indicated by our above structural analysis, the addition of Rab11a or RILPL2-RH1 shows a very limited capacity in activating MyoVa (Fig. 5C), suggesting that neither Rab11a nor RILPL2, when alone, is sufficient to release the autoinhibited conformation of MyoVa.

Previous studies have suggested a synergistic effect of different types of cargo adaptors in activating MyoVa (25, 46). Considering the requirement of the multiple interdomain interfaces for the assembly of the closed state (Fig. 3), these cargo adaptors may cooperatively act on the different interfaces to open MyoVa. By the addition of different combinations of the adaptor proteins in the ATPase assay, we found that, compared with the less than 50% enhancement by the individual cargo adaptors, the combinations of either Mlph-GTBM and Rab11a or Mlph-GTBM and RILPL2-RH1 significantly enhanced the ATPase activity to ~80 to 90% of the full activity indicated by the MD(2IQs) fragment of MyoVa (Fig. 5G), supporting the cargo-mediated coactivation mechanism. However, the coactivation efficiency of the Rab11a and RILPL2-RH1 mixture is still at a low level (Fig. 5G), indicating that the disruption of the d-strand–mediated GTD dimer is indispensable for the activation of MyoVa. Consistently, either the V1437Q mutation that directly disrupts the GTD/d-strand interactions or the E1089K mutation that impairs the stabilizing effect of CC[C] on the GTD[L]/d-strand[R] interaction significantly potentiates the Rab11a-induced activation of MyoVa (fig. S11C), although the two mutations show no or modest interference on the autoinhibited activity of MyoVa (Fig. 3D).

Next, we tested the coactivation mechanism in HeLa cells. In line with the ATPase activity results, overexpressing either Spire1-GTBM or Rab11a alone cannot promote the peripheral distribution of MyoVa in the cells (Fig. 5H and fig. S11D). In contrast, cotransfection of Spire1-GTBM and Rab11a greatly enhanced MyoVa's puncta formation in cell periphery, similar to the cellular distribution of the fully active mutant MyoVa[D134K/D136K] (Fig. 5H and fig. S11D) and the previous observations of the activated MyoVa in A431 and HeLa cells (33, 34). This result indicates that MyoVa has been activated efficiently by the presence of both Spire1 and Rab11, consistent with the previous findings that Spire proteins regulate the MyoV-mediated Rab11-vesicle transport (25, 47). As a control, the L454Q mutant of Spire1-GTBM and the F48Q mutant of Rab11a, which lose the binding capability to GTD (fig. S11E) (41), failed to activate MyoVa in the cells (Fig. 5H and fig. S11D).

Calcium-mediated activation

It has been reported that Ca^{2+} at a micromolar level can stimulate MyoVa's ATPase activity in vitro (13–15). Calcium-mediated activation of MyoVa is mainly through CaM on the LAs. CaM1 has been proposed to undergo a large conformational change induced by Ca^{2+} binding (30). Our structural comparison showed that the C-lobe of the Ca^{2+}-bound CaM1 (Ca^{2+}-CaM1) clashes with the SD-II of the GTD in the closed state (fig. S12, A and B), indicating that the Ca^{2+}-induced conformational transition of the CaM1 disrupts the head/tail interaction and thereby may release the autoinhibition. Ca^{2+}-CaM1 also has clashes with CaM2 in our structure (fig. S12, A and C), suggesting that CaM2 may disassociate from the LA or change its conformation upon Ca^{2+} binding to make room for Ca^{2+}-CaM1. Consistently, CaM2 has been observed to be the first CaM dissociating from LA during the Ca^{2+}-induced MyoVa activation (48, 49). In addition, given the importance of the CaM6/CC interaction in the closed state formation (Fig. 3C), the Ca^{2+}-induced displacement of CaM6 is likely to release the CC from the hinge structure and thereby unfold the closed state (fig. S12, A and D). Together, Ca^{2+} binding to CaM, especially the CaM1, CaM2, and CaM6, may lead to the activation of MyoVa. Nevertheless, whether Ca^{2+}-CaM still provides enough rigidity for the LAs in the active MyoVa for the processive walking requires further investigations.

In the cells with ionomycin-induced Ca^{2+} influx, MyoVa was found to associate with vesicular structures and showed a punctate distribution, suggesting that MyoVa is activated by Ca^{2+} to load membranous cargos (33). Likewise, we observed that the overexpressed MyoVa in the HeLa cell tended to form puncta in response to the ionomycin treatment (fig. S12, E and F), similar to our observations of the active mutants in both HeLa cells and melanocytes (Fig. 3E and figs. S8C and S9D).

The closed states in other MyoVs

The autoinhibition mediated by the head/tail interaction has been found in the different members of the MyoVs, including vertebrate MyoVb and MyoVc (50, 51), *Drosophila* MyoV (52, 53), and yeast Myo2p (54). Therefore, the closed state observed here in mouse MyoVa may provide a general understanding of other MyoV members. Sequence alignments of the interface residues found in our closed MyoVa structure reveals that the head/tail interaction is highly conserved in the MyoVs across different species from human to yeast (fig. S13A). The high conservation between MyoVa and MyoVb in the interface residues of the GTD/d-strand, CC/CaM6, and CC/GTD interactions (fig. S13, B and C) supports the existence of a very similar triangular-shaped structure in MyoVb, which was further confirmed by negative stain EM and cryo-EM analyses (fig. S14, A and B). As MyoVb also bind to some GTBM-containing proteins and Rab11a (23, 25, 26, 41), it is likely that MyoVa and MyoVb share the same cargo-mediated activation mechanism.

On the other hand, the MyoVc orthologs lack some structural elements in the formation of the hinge structure, including the C-terminal half of IQ6, the hinge-strand, and the CC[N] (fig. S13B), implying that MyoVc either has a hinge structure different from MyoVa or is incapable of forming the triangular shape. Although the d-strand sequence is not found in yeast Myo2p (fig. S13C), considering the different cargo/GTD binding modes in Myo2p and

MyoVa (*55*, *56*), Myo2p-GTD may use a different regulation mechanism in response to cargo binding.

DISCUSSION

In summary, the closed state structure of MyoVa provides an atomic picture to elucidate the autoinhibition mechanism. Combining the biochemical and cellular analyses, we elaborate the molecular basis of the triangular structure through different intra-/interpolypeptide chain interactions in MyoVa and CaM, the blocked ATPase activity by the head/tail interaction, and the cargo-/calcium-mediated activation of the closed MyoVa. On the basis of our findings, we proposed an activation model for MyoVa upon cargo loading (Fig. 6). In this model, the inhibited MyoVa switches between the closed and "half-closed" conformations (Fig. 6, A and B). In the half-closed conformations, the MD vertices and the short side in the triangular structure become mobile (fig. S7, C and D), presumably caused by the dynamic association/dissociation between the GTD^R and the d-strand^L. Nevertheless, the MDs and GTDs likely maintain their association in the half-closed MyoVa. In the presence of the GTBM-containing proteins, the GTBM can replace the d-strand^L in binding

to the GTD^R, consistent with the previous proposed model (*23–25*). However, given the relatively strong GTD^L/d-strand^R interaction sheltered by the CC_C (Fig. 3B) and the nanomolar level of GTBM-containing proteins in the cells (*57*), the GTBM alone cannot effectively displace the d-strand^R from the GTD^L to open MyoVa, and thereby MyoVa remains mainly closed and inactive (Fig. 5, G and H). However, simultaneous bindings of different cargos (e.g., the GTBM-containing adaptors and Rab11a or RILPL2) to the GTD can synergize the release of the autoinhibited conformation of MyoVa by cooperatively disrupting the head/tail interaction (*25*) and allowing the MD^R and LA^R to move away from the GTD^R (Fig. 6C). Consequently, $CaM6^R$ releases the CC_N, leading to the deformation of the hinge structure at the bottom vertex (Fig. 6C). Once losing the two vertices, the triangular-shaped structure is unsustainable, and MyoVa is fully open and active (Fig. 6D). Conversely, once the cargos are unloaded at destination, the cargo-free MyoVa may fold back to the closed state again, driven by the multiple interdomain/intermolecular interactions observed in the autoinhibited conformation.

Despite the master role of MyoVa in intracellular transport, it remains largely a mystery how MyoVa picks the right cargos for
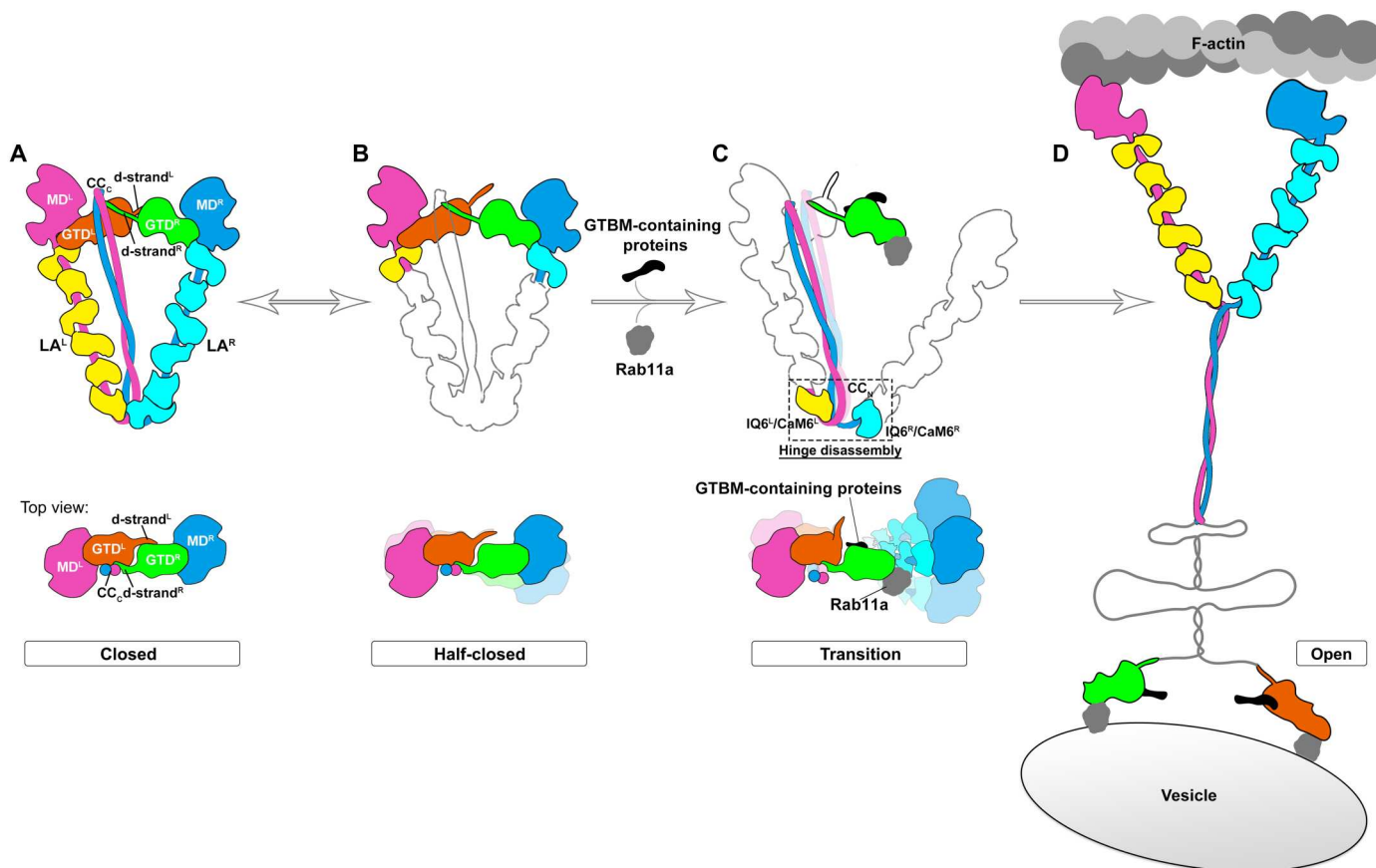

Fig. 6. A proposed activation model of MyoVa. (**A**) Closed state of MyoVa. The schematic drawing of this conformation is derived from the closed MyoVa-CaM^{4M} structure. (**B**) Half-closed state of MyoVa. The d-strand^L temporally dissociates from the GTD^R, leading to the dynamic conformation of the short side in the triangular-shaped structure. (**C**) "Transition" state of MyoVa. In the presence of both a GTBM-containing protein and Rab11a, the half-closed conformation undergoes a large motion of both the MD^R and the LA^R, resulting in the disassembly of the hinge structure. Notably, only one cargo binding of either GTBM-containing protein or Rab11a is not sufficient to effectively activate MyoVa. (**D**) Open state of MyoVa. The unstable transition conformation quickly shifts to the open conformation, allowing the GTDs to tightly associate with cargos and the MDs to hydrolyze ATP for the walking.

transport. In our model, cellular cargos simultaneously equipped with multiple correct cargo adaptors (e.g., a GTBM-containing adaptor and Rab11a) can activate MyoVa efficiently. Such a coincident activation prevents any individual, cargo-free adaptors or cargos without sufficient adaptors in either numbers or types, from improperly activating MyoVa, and effectively links the transport activity to the cargo specificity of the motor. However, since MyoVa transports a diverse array of vesicles/organelles, how can MyoVa be activated by other cargo adaptors, such as Rab6, Rab8, and Rab10 (33, 34)? Besides GTD, alternatively spliced exons in the tail region provide additional cargo-binding sites (33). These flexible exons are located near the GTD/d-strand interface, as indicated by the weak density in our EM map (Fig. 1B). It is likely that MyoVa reacts to the cargos coated with both the GTBM-containing adaptors and the exon-binding adaptors, in which the binding of adaptors to the exon region proximally enhances the GTBM binding and coactivates MyoVa. Nevertheless, we cannot rule out the possibility that these exons might be artificially cross-linked to the GTD dimer by GA treatment during cryo-EM sample preparation. Whether the exons in the closed MyoVa have a position near the GTD and whether the potential proximal effect of cargo binding plays a role in MyoVa activation require further investigations.

Compared with the extensive studies of the MD and GTD in MyoVa (12, 24, 36), the understanding of the CC has been largely limited to its function in the dimerization of two MyoVa heavy chains (10, 12). Our structure shows that the CC plays multiple roles in the closed state assembly and the activation of MyoVa. The long length of the CC allows its two ends to connect the bottom vertex (by interacting with CaM6) and the short side (by interacting with the GTD^L), respectively, supporting the triangular architecture of MyoVa (Fig. 3, B and C). The CC_N/CaM6 interaction is the basis of forming the hinge structure, while the CC_C/GTD^L interaction stabilizes the GTD^L/d-strand^R interaction and regulates MyoVa in the cargo-mediated activation (Fig. 6). Myosin II also relies on its long CC domain to adopt an autoinhibited structure with asymmetric features (58, 59). As many myosins and kinesins have a long CC domain (3, 60), the multiple regulatory roles of the CC found in our structure provide insights into the activity regulation mechanisms of various cytoskeletal motors. Furthermore, the approximately parallel association of the α-helices in the C-terminal CC region indicates the presence of perturbations of the heptad sequence repeat, similar to the "skip residue" that causes local parallel association in the smooth muscle myosin tail (58, 59).

Autoinhibition is a common feature of many unconventional myosins (e.g., myosin V, myosin VI, myosin VII, and myosin X) and kinesins (e.g., kinesin-1, kinesin-2, kinesin-3, and kinesin-7) to control their transport activity, and the head/tail interaction has been found in these autoinhibited motors (16, 20, 61–65). Our discoveries of the autoinhibition mechanism of MyoVa and the head/tail interaction in blocking ATPase activity may provide a general paradigm for the regulatory mechanisms underlying the intracellular movement of cytoskeletal motors.

MATERIALS AND METHODS

Plasmids
The genes of mouse MyoVa in brain isoform (containing exons A/B/C/E) and in skin isoform (containing exons A/C/D/E/F) and mouse MyoVb (without exon D) were codon-optimized and synthetized by GENEWIZ. For protein production, MyoVa brain isoform was introduced into a modified pFastbac-HTB vector with an N-terminal tandem His-Flag tag followed by a Tobacco Etch Virus (TEV) protease cleavage site, and MyoVb was constructed into pCAG vector with a His-Flag tag at N terminus. Mouse CaM gene was amplified from mouse complementary DNA library and cloned into pFastbac-HTB with an N-terminal His tag followed by a TEV protease cleavage site or pCAG vector with an N-terminal His tag. Human Rab11a (1 to 177), mouse Mlph-GTBM (170 to 208), and mouse RILPL2-RH1 (1 to 97) were recombined into a modified pET32a vector. For cellular assay in melanocytes or HeLa cells, MyoVa skin isoform was inserted into a modified pEGFP-C1 vector, and human Rab11a, human Spire1-GTBM (445 to 472), and mouse RILPL2-RH1 (1 to 97) were constructed into the vectors of pmCherry-C1, pEBFP-C1 [an exchange of green fluorescent protein (GFP) in pEGFP-C1 by blue fluorescent protein], and a modified pcDNA3.1 with 3*Flag at N terminus. All the mutants are produced by the QuickChange Site-Directed Mutagenesis Kit, and all the plasmids were sequenced for verification.

Protein expression and purification
To prepare the MyoVa-CaM complex, MyoVa or its V1437F mutant was coexpressed with CaM or CaM^{4M} (containing four mutations of E32Q, E68Q, E105Q, and E141Q that abolish Ca^{2+} binding) (15) in a baculovirus/insect cell expression system with the general Bac-to-Bac method. The $MyoVb-CaM^{4M}$ complex was obtained from cotransfection in mammalian human embryonic kidney 293F expression system. Both the cells with 3-day expression of the $MyoVa-CaM/CaM^{4M}$ or $MyoVb-CaM^{4M}$ complex were collected and washed with the phosphate-buffered saline buffer in supplement of 5 mM EGTA. The cells were then lysed by Dounce homogenizer at ice-bath in the lysis buffer [50 mM tris (pH 7.5), 300 mM NaCl, 5 mM $MgCl_2$, 5 mM ATP, 0.5% Triton X-100, 2 mM dithiothreitol (DTT), 1 mM EGTA, and protease inhibitors]. The supernatant, obtained by two-round centrifugation at the speed of 20,000 rpm, was loaded into anti-Flag beads (Smart-Lifesciences) followed by a 2-hour incubation. After extensive washing, the target protein was eluted with the lysis buffer without Triton X-100 supplemented with Flag peptide (500 μg/ml). After removing the tag by TEV protease overnight, the elution was further purified by size exclusion column (Superdex increase-6, GE) with the phosphate buffer [20 mM Na_2HPO_4/NaH_2PO_4 (pH 7.4), 60 mM NaCl, 1 mM EGTA, 1 mM DTT, and 2 mM $MgCl_2$] or the tris buffer [20 mM tris (pH 7.5), 80 mM NaCl, 1 mM EGTA, 1 mM DTT, and 2 mM $MgCl_2$]. Last, the peak fractions of $MyoVa/Vb-CaM^{4M}$ and MyoVa-CaM complexes were concentrated for cryo-EM and biochemical studies, respectively.

MyoVa-GTD (1444 to 1828), MyoVa-d-strand (1427 to 1445), MyoVa-d-strand + GTD (1419 to 1828), Rab11a (1 to 177), Mlph-GTBM (170 to 208), Spire1-GTBM (445 to 472), and RILPL2-RH1 (1 to 97) proteins were expressed in *Escherichia coli* BL21(DE3) expression system and purified by using Ni^{2+} column followed by a size exclusion column (Superdex 200, GE) with a

buffer of 50 mM tris (pH 7.5), 100 mM NaCl, and 1 mM DTT (41). The fractions containing target proteins were collected and concentrated followed by A280-based concentration measurement.

Negative staining EM

Protein sample (4 μl) was injected into a freshly glow-discharged grid. After 1-min incubation, the extra protein solution was removed by a filter paper, and 2% uranyl acetate was immediately dropped with a volume of 4 μl to stain for additional 40 s. The grid was then dried for testing. All the prepared grids were checked, and images were acquired in Talos L120C G2 (FEI) with 120-kV voltage.

GA cross-link

The closed MyoVa-CaM^{4M} complexes are easily disrupted to become the open conformation by freezing during preparation of cryo-sample (fig. S1D). To protect the closed particles, the cross-link method was applied (59). A final concentration of 0.1% GA was added to cross-link the samples with a concentration of ~0.5 mg/ml in the phosphate buffer for 1 min at room temperature. The reaction system was immediately terminated by adding a final concentration of 200 mM tris solution (pH 7.5). The cross-linked proteins were further purified by size-exclusion column (Superdex increase-6, GE) with the buffer containing 50 mM tris (pH 7.5), 80 mM NaCl, 1 mM EGTA, 1 mM DTT, and 2 mM MgCl$_2$. The target fractions were collected and concentrated for preparing cryo-samples. Similarly, the MyoVb-CaM^{4M} complex was also treated with GA cross-linking before cryo-EM experiments.

Grid preparation and cryo-EM data acquisition

The fresh purified complexes cross-linked by GA were concentrated to 0.3 to 0.5 mg/ml and further checked by negative staining EM. To prepare samples for cryo-EM study, 4 μl of each protein was applied onto a freshly glow-discharged grid (QUANTIFOIL Cu, 300 mesh, 1.2/1.3) with 5-s incubation and 5-s blotting with filter paper, and each grid was then quickly frozen into liquid ethane. The processes were performed by using Vitrobot (FEI) at 4°C with 95% or higher humidity. All the grids were stored in liquid nitrogen before screening and data collection.

Grids were transferred to a Titan Krios transmission electron microscope (Thermo Fisher Scientific) at 300 kV, equipped with a K3 direct electron detector. The movies of either MyoVa-CaM^{4M} or MyoVa^{V1437F}-CaM^{4M} were collected by using SerialEM 3.7 software (66) in four separated sections in counted super-resolution mode with a super-resolution pixel size of 0.536 Å and binned to 1.072 Å for data processing. Last, 33,865 movies for MyoVa-CaM^{4M} and 20,836 movies for MyoVa^{V1437F}-CaM^{4M} were obtained. Each movie is composed of 32 frames in 2.0-s exposure, and a total dose rate is 50 $e^-/Å^2$ per movie. The defocus range was set from −1.5 to −2.5 μm. Using similar procedures and settings, ~8000 movies of the MyoVb-CaM^{4M} complex were collected for 2D classification analysis.

Cryo-EM data processing

Each section of the two datasets of MyoVa-CaM^{4M} and MyoVa^{V1437F}-CaM^{4M} were processed separately in the procedures of motion-correction, contrast transfer function (CTF) estimation, particle picking, 2D classification, and initial 3D classification. Similarly, the movies in each section were aligned by using MotionCor2 (67) or Patch motion correction in cryoSPARC V3.1.0 (68) with a B-

factor of 150 to generate the micrographs with a physical pixel size of 1.072 Å, then the defocus of each micrograph was estimated by CTFFIND4 with amplitude contrast of 0.1 (69), and all the micrographs were manually selected to remove the junk micrographs. All the following processes were performed in cryoSPARC V3.1.0 (68). For MyoVa-CaM^{4M} complex, at first, 2048 particles were manually picked, and the good classes from 2D classification were used as reference for template-based auto-picking in the first-section dataset. Again, the good classes from 2D classification results of the first section were selected as reference to template-based auto-pick the particles in the following section datasets, followed by three rounds of 2D classification and one round of 3D classification. Then, the particles with a "V" shape were merged for another several rounds of 3D classification, and last, the particles with a relatively complete triangle shape were collected. After removing the duplicated particles with a minimal distance of 150 Å, a density map with 5.90-Å resolution of MyoVa-CaM^{4M} was generated by using nonuniform refinement, followed by local refinement with a manually created mask. In above processes, the box size for the extracted particles is 600×600 pixels. However, to reduce the particle size and save the calculation source, we binned the particles by four times in 2D classification and first round of 3D classification and binned by two times in the following rounds of 3D classification. Similar procedures for data processing were performed in the dataset of MyoVa^{V1437F}-CaM^{4M}, except that we initially used the results of MyoVa-CaM^{4M} 2D classfication as references for template-based auto-picking. As a result, a density map of 4.95-Å resolution was generated in cryoSPARC V3.1.0 software.

Considering the identical conformation of MyoVa-CaM^{4M} and MyoVa^{V1437F}-CaM^{4M} in the closed state, we combined two datasets to further improve the density map. After one round of 2D classification followed by one round of 3D classification, we selected 160,273 particles from three better classes, and last, we generated a density map of 4.78-Å resolution for the MyoVa-CaM^{4M} complex. Considering the high flexibility of the MyoVa-CaM^{4M} complex, we created the masks followed by particle subtraction and local refinement to improve the local density quality by focusing on the three subregions, in which the subregion 1 contains MD^L, GTD^L, and CC$_C$; the subregion 2 contains MD^R and GTD^R; and the subregion 3 contains two IQ5/CaM5, two IQ6/CaM6, and CC$_N$. The density maps of the three subregions were improved to the resolution of 4.10, 4.06, and 4.58 Å, respectively. Notably, the gold standard Fourier shell correlation (FSC) of 0.143 was used to cutoff the resolution for all our cryo-EM maps generated in this study (table S1). Similar procedures were applied to process the collected movies of the MyoVb-CaM^{4M} complex for 2D classification analysis, except that the 2D classes of MyoVa-CaM^{4M} complex were selected as references for template-based particle picking.

Model building and refinement

To obtain an atomic model for the closed MyoVa-CaM^{4M} complex, we first created a rough model by simply rigid body fitting the crystal structures of MD in rigor state [Protein Data Bank (PDB) ID: 1OE9 for MD$^{L/R}$] (27), GTD (PDB ID: 3WB8 for GTD$^{L/R}$) (26), and IQ/CaM (PDB ID: 2IX7 for LA$^{L/R}$) (28) into the overall map of full-length MyoVa-CaM^{4M} complex in UCSF Chimera software (70). Also, the d-strand$^{L/R}$ regions were generated with the reference of the crystal structure of the MyoVa-GTD/Mlph-GTBM complex (PDB ID: 4KP3) (26). In addition, the AlphaFold2-

predicted CC structures of the residues 910 to 1110 (29), all of which display a conserved architecture containing two N-terminal regular superhelices and a C-terminal parallel-like structure, were used to model the CC region. Next, three separated maps of the subregions with better resolution were used to assist the refinement of three submodels, respectively. After the manual adjustments in Coot (71), the three submodels were subjected into real-space refinement in Phenix, respectively (72). Then, the refined submodels were merged on the basis of the overall density map. In this stage, IQ2-4/CaM2-4 and the middle part of CC that are excluded in the three submodels were manually adjusted in Coot. The crystal structures and AlphaFold2-based model mentioned above were also used to guide the assignment of side chains. Last, the merged model was further improved by real-space refinement with a relative tight restraint and then validated in Phenix by fitting with the overall density map (table S1). Figures containing structural display and analysis were prepared using UCSF Chimera, UCSF ChimeraX (73), and PyMOL (www.pymol.org).

Isothermal titration calorimetry

ITC measurements were performed on a PEAQ-ITC Microcal calorimeter (Malvern). The GTBM or d-strand variants were prepared with a concentration of 400 μM in the syringe and the MyoVa-GTD fragment with a concentration of 40 μM in the cell. All the protein samples were prepared in the same buffer condition of 50 mM tris (pH 7.5), 100 mM NaCl, 1 mM DTT, and 1 mM EDTA. The titration was processed by injecting 3 μl of sample in the syringe to the cell each time. An interval of 150 s between two injections was set to ensure the curve back to the baseline. The titration data were analyzed and fitted by a one-site binding model.

Analytical gel filtration

The samples with a volume of 100 μl were prepared in a final concentration of 60 μM and loaded onto a Superdex 200 Increase 10/300 GL or Superdex 6 Increase column (GE Healthcare) on an ÄKTA pure system (GE Healthcare), equilibrated with the same buffer used in protein purification.

ATPase assay

An ATP regeneration system was used to measure the ATPase activity of MyoVa as previously reported (13). Briefly, the ATPase activity was measured at 25°C in a solution containing 50 mM tris (pH 7.5), 1 mM $MgCl_2$, bovine serum albumin (0.25 mg/ml), 1 mM DTT, 2.5 mM phosphoenolpyruvate, pyruvate kinase (20 U/ml), 80 mM NaCl, 1 mM EGTA, 10 μM actin, and 100 nM MyoVa-CaM or the mutants. For the cargo-mediated activation assay, each cargo adaptor was added with the indicated concentration, and 1 mM guanosine triphosphatase was supplied in the reactions containing Rab11a. The reaction was initialized by adding 0.5 mM ATP. After 5 min, the reaction was terminated by adding 20 μl of reaction solution into the stop buffer containing 70 μl of 0.36 mM 2,4-dinitrophenyl hydrazine and 0.4 M HCl at each 15-min interval between 5 and 65 min. After incubation of the mixture at 37°C for 15 min, 50 μl of color buffer of 2.5 M NaOH and 0.1 M EDTA was added, and A460 absorption was detected. The velocity of the reaction was measured by the liner-fit slope between A460 absorption and reaction time. For the mutagenesis and coactivation assay, the ATPase activity was normalized to that of the wild-type MyoVa for fold change calculation of the basal activity. For cargo concentration-dependent activation assay, ATPase activity was normalized between 0 and 100%, referring to the activity of the closed MyoVa and the fully active fragment, MD(2IQs), respectively.

CRISPR-Cas9–mediated generation of MyoVa knockout cell line in melanocytes

MyoVa knockout (MyoVa[KO]) melanocytes were derived from mouse melanocytes B16F10, and the generation is based on a CRISPR-Cas9–mediated gene editing system (74). In brief, the guide RNA targeting to the sequences of 5′-TGGAATCGATGAA GCGAACT-3′ was designed and inserted into the plasmid pSpCas9(BB)-2A-GFP (PX458; Addgene, #48138). The plasmid was transfected into mouse melanocytes, and the single cell with GFP-positive signal was sorted into 96-well plates with each well containing single colony by fluorescence-activated cell sorter (FACS; BD FACS AriaTMIII). After cell propagation, the MyoVa[KO] melanocytes were detected and confirmed by Western blotting, immunofluorescence, and sequencing.

Cell culture and transfection

Mouse melanocytes B16F10, MyoVa[KO] melanocytes, and human HeLa cells were cultured in Dulbecco's modified Eagle's medium (Corning) supplemented with 10% fetal bovine serum and penicillin/streptomycin (100 U/ml) in 5% CO_2 condition at 37°C. Transfection was performed using Lipofectamine 3000 (Thermo Fisher Scientific), according to the manufacturer's instructions.

Immunofluorescence, imaging, and analysis

MyoVa[KO] melanocytes and HeLa cells were transfected/cotransfected with the plasmids as indicated. After 24-hour transfection, the cells were detached by trypsin treatment and seeded onto fibronectin-coated coverslips for additional 24 hours. Then, the cells were fixed with 4% paraformaldehyde for 15 min and treated with 0.1% Triton X-100 for another 15 min at room temperature. Actin was stained with Alexa Fluor 647 phalloidin dye (Thermo Fisher Scientific). Confocal images of the cells were acquired with the same confocal settings by a Nikon A1 microscope (Nikon, Japan).

MyoVa puncta intensity analysis was performed in the Surpass module of Imaris software. The cells were bounded with the stained F-actin, and a same threshold was used to filter out the punctate structures of GFP-MyoVa in all the cells. The intensity ratio of the punctate MyoVa to the overall MyoVa was calculated to indicate the puncta formation of MyoVa.

Melanosome distribution analysis

Cell edge and nucleus were bounded by the stained actin and 4′,6-diamidino-2-phenylindole (DAPI), respectively. The distance of each melanosome to the center of cell nucleus was calculated and normalized to the distance from the center of the nucleus to the cell edge across this melanosome. The melanosomes with a normalized distance of more than 0.5 were considered to locate in the peripheral region of melanocytes. The percentage of melanosomes in the peripheral region was calculated to indicate the degree of melanosome dispersion in each melanocyte.

Statistical analysis

The ATPase activity values are displayed with an error bar of standard deviation for three independent experiments, and the cellular analyses are displayed as violin plot with the median and quartiles

for each condition. Significance was calculated using unpaired, two-tailed and nonparametric Mann-Whitney test for cellular results and using unpaired, two-tailed and parametric *t* test for ATPase activity, respectively. In all statistical tests, $P > 0.05$ was considered as not significant (ns), while $P < 0.05$ was indicated as "*," $P < 0.01$ as "**," $P < 0.001$ as "***," and $P < 0.0001$ as "****." All the statistical analysis was performed by using the Prism 9.0 software.

Supplementary Materials

This PDF file includes:
Figs. S1 to S14
Tables S1 and S2

Other Supplementary Material for this manuscript includes the following:
Movie S1

REFERENCES AND NOTES

1. M. A. Hartman, D. Finan, S. Sivaramakrishnan, J. A. Spudich, Principles of unconventional myosin function and targeting. *Annu. Rev. Cell Dev. Biol.* **27**, 133–155 (2011).
2. N. Hirokawa, R. Takemura, Molecular motors and mechanisms of directional transport in neurons. *Nat. Rev. Neurosci.* **6**, 201–214 (2005).
3. N. Hirokawa, S. Niwa, Y. Tanaka, Molecular motors in neurons: Transport mechanisms and roles in brain function, development, and disease. *Neuron* **68**, 610–638 (2010).
4. M. Kneussel, W. Wagner, Myosin motors at neuronal synapses: Drivers of membrane transport and actin dynamics. *Nat. Rev. Neurosci.* **14**, 233–247 (2013).
5. R. D. Vale, The molecular motor toolbox for intracellular transport. *Cell* **112**, 467–480 (2003).
6. J. A. Hammer III, J. R. Sellers, Walking to work: Roles for class V myosins as cargo transporters. *Nat. Rev. Mol. Cell Biol.* **13**, 13–26 (2012).
7. A. D. Mehta, R. S. Rock, M. Rief, J. A. Spudich, M. S. Mooseker, R. E. Cheney, Myosin-V is a processive actin-based motor. *Nature* **400**, 590–593 (1999).
8. E. Pastural, F. J. Barrat, R. DufourcqLagelouse, S. Certain, O. Sanal, N. Jabado, R. Seger, C. Griscelli, A. Fischer, G. de Saint Basile, Griscelli disease maps to chromosome 15q21 and is associated with mutations in the myosin-Va gene. *Nat. Genet.* **16**, 289–292 (1997).
9. T. Muller, M. W. Hess, N. Schiefermeier, K. Pfaller, H. L. Ebner, P. Heinz-Erian, H. Ponstingl, J. Partsch, B. Rollinghoff, H. Kohler, T. Berger, H. Lenhartz, B. Schlenck, R. J. Houwen, C. J. Taylor, H. Zoller, S. Lechner, O. Goulet, G. Utermann, F. M. Ruemmele, L. A. Huber, A. R. Janecke, MYO5B mutations cause microvillus inclusion disease and disrupt epithelial cell polarity. *Nat. Genet.* **40**, 1163–1165 (2008).
10. S. L. Reck-Peterson, D. W. Provance, M. S. Mooseker, J. A. Mercer, Class V myosins. *Biochim. Biophys. Acta Cell Res.* **1496**, 36–51 (2000).
11. M. Van Gele, P. Dynoodt, J. Lambert, Griscelli syndrome: A model system to study vesicular trafficking. *Pigment Cell Melanoma Res.* **22**, 268–282 (2009).
12. K. M. Trybus, Myosin V from head to tail. *Cell. Mol. Life Sci.* **65**, 1378–1389 (2008).
13. X. D. Li, K. Mabuchi, R. Ikebe, M. Ikebe, Ca^{2+}-induced activation of ATPase activity of myosin Va is accompanied with a large conformational change. *Biochem. Biophys. Res. Commun.* **315**, 538–545 (2004).
14. F. Wang, K. Thirumurugan, W. F. Stafford, J. A. Hammer, P. J. Knight, J. R. Sellers, Regulated conformation of myosin V. *J. Biol. Chem.* **279**, 2333–2336 (2004).
15. D. N. Krementsov, E. B. Krementsova, K. M. Trybus, Myosin V: Regulation by calcium, calmodulin, and the tail domain. *J. Cell Biol.* **164**, 877–886 (2004).
16. K. Thirumurugan, T. Sakamoto, J. A. Hammer III, J. R. Sellers, P. J. Knight, The cargo-binding domain regulates structure and activity of myosin 5. *Nature* **442**, 212–215 (2006).
17. X. D. Li, H. S. Jung, K. Mabuchi, R. Craig, M. Ikebe, The globular tail domain of myosin Va functions as an inhibitor of the myosin Va motor. *J. Biol. Chem.* **281**, 21789–21798 (2006).
18. X. D. Li, H. S. Jung, Q. Z. Wang, R. Ikebe, R. Craig, M. Ikebe, Correction for Li *et al.*, The globular tail domain puts on the brake to stop the ATPase cycle of myosin Va. *Proc. Natl. Acad. Sci. U.S.A.* **105**, 3658–3658 (2008).
19. W. B. Zhang, L. L. Yao, X. D. Li, The globular tail domain of myosin-5a functions as a dimer in regulating the motor activity. *J. Biol. Chem.* **291**, 13571–13579 (2016).
20. J. Liu, D. W. Taylor, E. B. Krementsova, K. M. Trybus, K. A. Taylor, Three-dimensional structure of the myosin V inhibited state by cryoelectron tomography. *Nature* **442**, 208–211 (2006).
21. J. R. Sellers, K. Thirumurugan, T. Sakamoto, J. A. Hammer, P. J. Knight, Calcium and cargoes as regulators of myosin 5a activity. *Biochem. Biophys. Res. Commun.* **369**, 176–181 (2008).
22. A. F. Z. Nascimento, D. M. Trindade, C. C. C. Tonoli, P. O. de Giuseppe, L. H. P. Assis, R. V. Honorato, P. S. L. de Oliveira, P. Mahajan, N. A. Burgess-Brown, F. von Delft, R. E. Larson, M. T. Murakami, Structural insights into functional overlapping and differentiation among myosin V motors. *J. Biol. Chem.* **288**, 34131–34145 (2013).
23. O. Pylypenko, W. Attanda, C. Gauquelin, M. Lahmani, D. Coulibaly, B. Baron, S. Hoos, M. A. Titus, P. England, A. M. Houdusse, Structural basis of myosin V Rab GTPase-dependent cargo recognition. *Proc. Natl. Acad. Sci. U.S.A.* **110**, 20443–20448 (2013).
24. N. Zhang, L. L. Yao, X. D. Li, Regulation of class V myosin. *Cell. Mol. Life Sci.* **75**, 261–273 (2018).
25. O. Pylypenko, T. Welz, J. Tittel, M. Kollmar, F. Chardon, G. Malherbe, S. Weiss, C. I. L. Michel, A. Samol-Wolf, A. T. Grasskamp, A. Hume, B. Goud, B. Baron, P. England, M. A. Titus, P. Schwille, T. Weidemann, A. Houdusse, E. Kerkhoff, Coordinated recruitment of Spir actin nucleators and myosin V motors to Rab11 vesicle membranes. *eLife* **5**, (2016).
26. Z. Y. Wei, X. T. Liu, C. Yu, M. J. Zhang, Structural basis of cargo recognitions for class V myosins. *Proc. Natl. Acad. Sci. U.S.A.* **110**, 11314–11319 (2013).
27. P. D. Coureux, A. L. Wells, J. Menetrey, C. M. Yengo, C. A. Morris, H. L. Sweeney, A. Houdusse, A structural state of the myosin V motor without bound nucleotide. *Nature* **425**, 419–423 (2003).
28. A. Houdusse, J. F. Gaucher, E. Krementsova, S. Mui, K. M. Trybus, C. Cohen, Crystal structure of apo-calmodulin bound to the first two IQ motifs of myosin V reveals essential recognition features. *Proc. Natl. Acad. Sci. U.S.A.* **103**, 19326–19331 (2006).
29. J. Jumper, R. Evans, A. Pritzel, T. Green, M. Figurnov, O. Ronneberger, K. Tunyasuvunakool, R. Bates, A. Zidek, A. Potapenko, A. Bridgland, C. Meyer, S. A. A. Kohl, A. J. Ballard, A. Cowie, B. Romera-Paredes, S. Nikolov, R. Jain, J. Adler, T. Back, S. Petersen, D. Reiman, E. Clancy, M. Zielinski, M. Steinegger, M. Pacholska, T. Berghammer, S. Bodenstein, D. Silver, O. Vinyals, A. W. Senior, K. Kavukcuoglu, P. Kohli, D. Hassabis, Highly accurate protein structure prediction with AlphaFold. *Nature* **596**, 583–589 (2021).
30. M. Shen, N. Zhang, S. D. Zheng, W. B. Zhang, H. M. Zhang, Z. K. Lu, Q. P. Su, Y. J. Sun, K. Q. Ye, X. D. Li, Calmodulin in complex with the first IQ motif of myosin-5a functions as an intact calcium sensor. *Proc. Natl. Acad. Sci. U.S.A.* **113**, E5812–E5820 (2016).
31. Z. K. Lu, M. Shen, Y. Cao, H. M. Zhang, L. L. Yao, X. D. Li, Calmodulin bound to the first IQ motif is responsible for calcium-dependent regulation of myosin 5a. *J. Biol. Chem.* **287**, 16530–16540 (2012).
32. N. Kodera, D. Yamamoto, R. Ishikawa, T. Ando, Video imaging of walking myosin V by high-speed atomic force microscopy. *Nature* **468**, 72–76 (2010).
33. A. J. Lindsay, F. Jollivet, C. P. Horgan, A. R. Khan, G. Raposo, M. W. McCaffrey, B. Goud, Identification and characterization of multiple novel Rab-myosin Va interactions. *Mol. Biol. Cell* **24**, 3420–3434 (2013).
34. J. T. Roland, L. A. Lapierre, J. R. Goldenring, Alternative splicing in class V myosins determines association with Rab10. *J. Biol. Chem.* **284**, 1213–1223 (2009).
35. A. Houdusse, H. L. Sweeney, How myosin generates force on actin filaments. *Trends Biochem. Sci.* **41**, 989–997 (2016).
36. J. Robert-Paganin, O. Pylypenko, C. Kikuti, H. L. Sweeney, A. Houdusse, Force generation by myosin motors: A structural perspective. *Chem. Rev.* **120**, 5–35 (2020).
37. P. D. Coureux, H. L. Sweeney, A. Houdusse, Three myosin V structures delineate essential features of chemo-mechanical transduction. *EMBO J.* **23**, 4527–4537 (2004).
38. S. F. Wulf, V. Ropars, S. Fujita-Becker, M. Oster, G. Hofhaus, L. G. Trabuco, O. Pylypenko, H. L. Sweeney, A. M. Houdusse, R. R. Schroder, Force-producing ADP state of myosin bound to actin. *Proc. Natl. Acad. Sci. U.S.A.* **113**, E1844–E1852 (2016).
39. S. Pospich, H. L. Sweeney, A. Houdusse, S. Raunser, High-resolution structures of the actomyosin-V complex in three nucleotide states provide insights into the force generation mechanism. *eLife* **10**, e73724 (2021).
40. O. Sato, X. D. Li, M. Ikebe, Myosin Va becomes a low duty ratio motor in the inhibited form. *J. Biol. Chem.* **282**, 13228–13239 (2007).
41. F. F. Niu, K. Sun, W. J. Wei, C. Yu, Z. Y. Wei, F-actin disassembly factor MICAL1 binding to Myosin Va mediates cargo unloading during cytokinesis. *Sci. Adv.* **6**, eabb1307 (2020).
42. L. L. Yao, Q. J. Cao, H. M. Zhang, J. Zhang, Y. Cao, X. D. Li, Melanophilin stimulates myosin-5a motor function by allosterically inhibiting the interaction between the head and tail of myosin-5a. *Sci. Rep.* **5**, 10874 (2015).
43. X. D. Li, R. Ikebe, M. Ikebe, Activation of myosin Va function by melanophilin, a specific docking partner of myosin Va. *J. Biol. Chem.* **280**, 17815–17822 (2005).
44. S. S. Correia, S. Bassani, T. C. Brown, M. F. Lise, D. S. Backos, A. El-Husseini, M. Passafaro, J. A. Esteban, Motor protein-dependent transport of AMPA receptors into spines during long-term potentiation. *Nat. Neurosci.* **11**, 457–466 (2008).
45. M. F. Lise, D. P. Srivastava, P. Arstikaitis, R. L. Lett, R. Sheta, V. Viswanathan, P. Penzes, T. P. O'Connor, A. El-Husseini, Myosin-Va-interacting protein, RILPL2, controls cell shape and neuronal morphogenesis via Rac signaling. *J. Cell Sci.* **122**, 3810–3821 (2009).

46. Q. J. Cao, N. Zhang, R. Zhou, L. L. Yao, X. D. Li, The cargo adaptor proteins RILPL2 and melanophilin co-regulate myosin-5a motor activity. *J. Biol. Chem.* **294**, 11333–11341 (2019).

47. M. Schuh, An actin-dependent mechanism for long-range vesicle transport. *Nat. Cell Biol.* **13**, 1431–1436 (2011).

48. H. Koide, T. Kinoshita, Y. Tanaka, S. Tanaka, N. Nagura, G. M. Z. Horste, A. Miyagi, T. Ando, Identification of the single specific IQ motif of myosin V from which calmodulin dissociates in the presence of Ca^{2+}. *Biochemistry* **45**, 11598–11604 (2006).

49. K. M. Trybus, M. I. Gushchin, H. Lui, L. Hazelwood, E. B. Krementsova, N. Volkmann, D. Hanein, Effect of calcium on calmodulin bound to the IQ motifs of myosin V. *J. Biol. Chem.* **282**, 23316–23325 (2007).

50. Z. Wang, J. G. Edwards, N. Riley, D. W. Provance Jr., R. Karcher, X. D. Li, I. G. Davison, M. Ikebe, J. A. Mercer, J. A. Kauer, M. D. Ehlers, Myosin Vb mobilizes recycling endosomes and AMPA receptors for postsynaptic plasticity. *Cell* **135**, 535–548 (2008).

51. L. L. Yao, M. Shen, Z. K. Lu, M. Ikebe, X. D. Li, Identification of the isoform-specific inter-actions between the tail and the head of class V myosin. *J. Biol. Chem.* **291**, 8241–8250 (2016).

52. H. H. Ji, H. M. Zhang, M. Shen, L. L. Yao, X. D. Li, The motor function of Drosophila mela-nogaster myosin-5 is activated by calcium and cargo-binding protein dRab11. *Biochem. J.* **469**, 135–144 (2015).

53. W. Lu, M. Lakonishok, R. Liu, N. Billington, A. Rich, M. Glotzer, J. R. Sellers, V. I. Gelfand, Competition between kinesin-1 and myosin-V defines *Drosophila* posterior determination. *eLife* **9**, e54216 (2020).

54. K. W. Donovan, A. Bretscher, Head-to-tail regulation is critical for the in vivo function of myosin V. *J. Cell Biol.* **209**, 359–365 (2015).

55. P. T. Eves, Y. Jin, M. Brunner, L. S. Weisman, Overlap of cargo binding sites on myosin V coordinates the inheritance of diverse cargoes. *J. Cell Biol.* **198**, 69–85 (2012).

56. K. Tang, Y. J. Li, C. Yu, Z. Y. Wei, Structural mechanism for versatile cargo recognition by the yeast class V myosin Myo2. *J. Biol. Chem.* **294**, 5896–5906 (2019).

57. N. H. Cho, K. C. Cheveralls, A.-D. Brunner, K. Kim, A. C. Michaelis, P. Raghavan, H. Kobayashi, L. Savy, J. Y. Li, H. Canaj, J. Y. S. Kim, E. M. Stewart, C. Gnann, F. McCarthy, J. P. Cabrera, R. M. Brunetti, B. B. Chhun, G. Dingle, M. Y. Hein, B. Huang, S. B. Mehta, J. S. Weissman, R. Gómez-Sjöberg, D. N. Itzhak, L. A. Royer, M. Mann, M. D. Leonetti, OpenCell: Endogenous tagging for the cartography of human cellular organization. *Science* **375**, eabi6983 (2022).

58. C. A. Scarff, G. Carrington, D. Casas-Mao, J. M. Chalovich, P. J. Knight, N. A. Ranson, M. Peckham, Structure of the shutdown state of myosin-2. *Nature* **588**, 515–520 (2020).

59. S. X. Yang, P. Tiwari, K. H. Lee, O. Sato, M. Ikebe, R. Padron, R. Craig, Cryo-EM structure of the inhibited (10S) form of myosin II. *Nature* **588**, 521–525 (2020).

60. H. L. Sweeney, E. L. F. Holzbaur, Motor proteins. *Cold Spring Harb. Perspect. Biol.* **10**, a021931 (2018).

61. I. Lister, S. Schmitz, M. Walker, J. Trinick, F. Buss, C. Veigel, J. Kendrick-Jones, A monomeric myosin VI with a large working stroke. *EMBO J.* **23**, 1729–1738 (2004).

62. Y. Yang, T. G. Baboolal, V. Siththanandan, M. Chen, M. L. Walker, P. J. Knight, M. Peckham, J. R. Sellers, A FERM domain autoregulates Drosophila myosin 7a activity. *Proc. Natl. Acad. Sci. U.S.A.* **106**, 4189–4194 (2009).

63. N. Umeki, H. S. Jung, S. Watanabe, T. Sakai, X. D. Li, R. Ikebe, R. Craig, M. Ikebe, The tail binds to the head-neck domain, inhibiting ATPase activity of myosin VIIA. *Proc. Natl. Acad. Sci. U.S.A.* **106**, 8483–8488 (2009).

64. N. Umeki, H. S. Jung, T. Sakai, O. Sato, R. Ikebe, M. Ikebe, Phospholipid-dependent regu-lation of the motor activity of myosin X. *Nat. Struct. Mol. Biol.* **18**, 783–788 (2011).

65. K. J. Verhey, J. W. Hammond, Traffic control: Regulation of kinesin motors. *Nat. Rev. Mol. Cell Biol.* **10**, 765–777 (2009).

66. D. N. Mastronarde, Automated electron microscope tomography using robust prediction of specimen movements. *J. Struct. Biol.* **152**, 36–51 (2005).

67. S. Q. Zheng, E. Palovcak, J. P. Armache, K. A. Verba, Y. F. Cheng, D. A. Agard, MotionCor2: Anisotropic correction of beam-induced motion for improved cryo-electron microscopy. *Nat. Methods* **14**, 331–332 (2017).

68. A. Punjani, J. L. Rubinstein, D. J. Fleet, M. A. Brubaker, cryoSPARC: Algorithms for rapid unsupervised cryo-EM structure determination. *Nat. Methods* **14**, 290–296 (2017).

69. A. Rohou, N. Grigorieff, CTFFIND4: Fast and accurate defocus estimation from electron micrographs. *J. Struct. Biol.* **192**, 216–221 (2015).

70. E. F. Pettersen, T. D. Goddard, C. C. Huang, G. S. Couch, D. M. Greenblatt, E. C. Meng, T. E. Ferrin, UCSF Chimera—A visualization system for exploratory research and analysis. *J. Comput. Chem.* **25**, 1605–1612 (2004).

71. P. Emsley, B. Lohkamp, W. G. Scott, K. Cowtan, Features and development of Coot. *Acta Crystallogr. D Biol. Crystallogr.* **66**, 486–501 (2010).

72. D. Liebschner, P. V. Afonine, M. L. Baker, G. Bunkoczi, V. B. Chen, T. I. Croll, B. Hintze, L.-W. Hung, S. Jain, A. J. McCoy, N. W. Moriarty, R. D. Oeffner, B. K. Poon, M. G. Prisant, R. J. Read, J. S. Richardson, D. C. Richardson, M. D. Sammito, O. V. Sobolev, D. H. Stockwell, T. C. Terwilliger, A. G. Urzhumtsev, L. L. Videau, C. J. Williams, P. D. Adams, Macromolecular structure determination using x-rays, neutrons and electrons: Recent developments in Phenix. *Acta Crystallogr. D* **75**, 861–877 (2019).

73. E. F. Pettersen, T. D. Goddard, C. C. Huang, E. C. Meng, G. S. Couch, T. I. Croll, J. H. Morris, T. E. Ferrin, UCSF ChimeraX: Structure visualization for researchers, educators, and devel-opers. *Protein Sci.* **30**, 70–82 (2021).

74. F. A. Ran, P. D. Hsu, J. Wright, V. Agarwala, D. A. Scott, F. Zhang, Genome engineering using the CRISPR-Cas9 system. *Nat. Protoc.* **8**, 2281–2308 (2013).